NACA

RESEARCH MEMORANDUM

SOME EXAMPLES OF THE APPLICATIONS OF THE TRANSONIC AND SUPERSONIC AREA RULES TO THE PREDICTION OF WAVE DRAG

By Robert L. Nelson and Clement J. Welsh

Langley Aeronautical Laboratory
Langley Field, Va.

NATIONAL ADVISORY COMMITTEE
FOR AERONAUTICS

WASHINGTON
March 20, 1957

NATIONAL ADVISORY COMMITTEE FOR AERONAUTICS

RESEARCH MEMORANDUM

SOME EXAMPLES OF THE APPLICATIONS OF THE TRANSONIC AND SUPERSONIC AREA RULES TO THE PREDICTION OF WAVE DRAG

By Robert L. Nelson and Clement J. Welsh

SUMMARY

The experimental wave drags of bodies and wing-body combinations over a wide range of Mach numbers are compared with the computed drags utilizing a 24-term Fourier series application of the supersonic area rule and with the results of equivalent-body tests.

The results indicate that the equivalent-body technique provides a good method for predicting the wave drag of certain wing-body combinations at and below a Mach number of 1. At Mach numbers greater than 1, the equivalent-body wave drags can be misleading. The wave drags computed using the supersonic area rule are shown to be in best agreement with the experimental results for configurations employing the thinnest wings. The wave drags for the bodies of revolution presented in this report are predicted to a greater degree of accuracy by using the frontal projections of oblique areas than by using normal areas. A rapid method of computing wing area distributions and area-distribution slopes is given in an appendix.

INTRODUCTION

The area rule, first advanced by Whitcomb in reference 1, has considerably altered the methods for predicting wave drag of wing-body combinations. Studies leading to the discovery of the area rule showed that interference drag between wing and body components could be very large. Therefore, estimation of drag by component buildup without somehow evaluating the interference drag could give misleading answers. However, in consequence of the transonic area rule, a valuable tool was made available to the designers in assessing the transonic drag. This was the equivalent-body concept, which states that at transonic speeds the pressure drag of the airplane is the same as that for a body of revolution

having the same longitudinal distribution of cross-sectional area. As a result, the drag of the configuration is obtained by either estimating or experimentally determining the equivalent-body drag. Experimental checks for airplane configurations presented in reference 2 generally support this concept in the transonic speed range.

The supersonic area rule, given by Jones in reference 3, provided a powerful method for calculating the wave drag at supersonic speeds. In references 4 and 5 the mechanics of the drag calculations were discussed together with a number of comparisons of calculated and experimental drags generally at low supersonic speeds. Jones pointed out in reference 3 that the method could be expected to give good results for thin wings mounted on vertically symmetrical bodies. Later, Lomax in reference 6 gave the complete linearized theory expressions for the drag. The added terms in Lomax's result represented the limitation pointed out by Jones.

The purpose of the present paper is to provide a better feel for the range of applicability of both the transonic and supersonic area rules. For the transonic area rule, this is done by making additional comparisons between equivalent-body and wing-body experiments. For the supersonic area rule, comparisons are made of calculated and experimental results for both body and wing-body combinations over a wider range of Mach numbers than heretofore made. The supersonic-area-rule calculations were made by using a 24-term Fourier series expression for the slope of the area distribution.

SYMBOLS

A frontal projection of the area cut by a Mach plane or wing aspect ratio

$$a_n = \frac{2}{\pi}\int_0^{\pi}\left(\frac{dA}{dx} - \frac{\beta}{2}\frac{f}{q}\right)\sin n\phi \, d\phi$$

C_D drag coefficient, $\frac{D}{qS}$

C_p pressure coefficient

c wing local chord

c_0 root chord of particular pointed wing tip

c_r wing root chord

c_t wing tip chord

D drag

d maximum body diameter, $2r_m$

f resultant pressure force

$f(\nu)$ wing-thickness-distribution function, $\frac{z}{z_{max}}$

$G(K,\nu_0)$ wing-area-distribution function

$H(K,\nu_0)$ wing-area-distribution slope function

K $m\left(1 + \frac{\beta \cos \theta}{\tan \Lambda}\right)$ for the left-wing panel; $m\left(1 - \frac{\beta \cos \theta}{\tan \Lambda}\right)$ for the right-wing panel

l length of configuration

l_t total length of area distribution

l/d body fineness ratio

M Mach number

$m = \frac{A}{4} \frac{(1 + \lambda)}{(1 - \lambda)} \tan \Lambda$

n integer

q dynamic pressure

r local body radius

r_m maximum body radius

S reference area

S_b body frontal area

S_e wing exposed area

S_w wing total plan-form area

s wing semispan

s_0 semispan of particular pointed-tip wing

t/c wing thickness ratio, $\frac{2z_{max}}{c}$

x,y,z Cartesian coordinates

x_0 point of intersection of Mach plane with the x-axis

x' x-coordinate measured from wing leading edge

x_1 dummy variable

z_{max} local maximum wing ordinate

$\beta = \sqrt{M^2 - 1}$

$\eta = \frac{y}{s}$

$\phi = \cos^{-1}\left(2 \frac{x}{l_t} - 1\right)$

Λ wing leading-edge sweepback angle

λ wing taper ratio, $\frac{c_t}{c_r}$

μ Mach angle, $\sin^{-1} \frac{1}{M}$

$\nu = \frac{x'}{c}$

ν_0 value of ν at root of particular pointed-tip wing

ν_r value of ν at root of actual wing

θ angle between z-axis and line of intersection of Mach plane with the y,z plane

REVIEW OF THE BASIC THEORY

From reference 6, the equation for the wave drag of any system of bodies or wings and bodies can be written as:

$$\frac{D}{q} = -\frac{1}{4\pi^2}\int_0^{2\pi} d\theta \int_0^{l_t} dx \int_0^{l_t} dx_1 \left[\frac{d^2A(x,\theta)}{dx^2} - \frac{\beta}{2q}\frac{df(x,\theta)}{dx}\right]\left[\frac{d^2A(x_1,\theta)}{dx_1^2} - \frac{\beta}{2q}\frac{df(x_1,\theta)}{dx_1}\right]\log(x - x_1) \qquad (1)$$

The equation is subject to the usual limitations of the linearized theory.

Before discussing the terms in the drag equation, it is well to review the definition of Mach planes. The physical significance of equation (1) is understood if the configuration is cut by Mach planes. Mach planes are easily visualized by considering a Mach cone originating at a point on the x-axis which is alined with the remote relative wind. A Mach plane is simply a plane tangent to the Mach cone and at an angle of roll, θ about the x-axis measured from the y-axis. By moving the vertex of the Mach cone along the x-axis, a series of parallel Mach planes will cut the configuration for a fixed roll angle θ.

In the drag equation the term $A(x,\theta)$ represents the frontal projection of the oblique area cut by a particular Mach plane, whereas $f(x,\theta)$ represents the net force normal to the stream direction on this section in the θ direction. These relationships are illustrated in figure 1 for angle of roll θ of the Mach plane of 0° and 90°. By neglecting the term $\frac{\beta}{2q}\frac{df(x,\theta)}{dx}$, the equation reduces to the supersonic-area-rule formula given by Jones in reference 3. Evaluation of $f(x,\theta)$ requires the pressure distribution on the configuration which when integrated over the configuration gives the drag directly. As a result, large values of $\frac{\beta}{2q}\frac{df(x,\theta)}{dx}$ impose a limitation on the supersonic area rule, even within the framework of the linearized theory.

It is not the purpose of the present paper to evaluate the drag of configurations including the effect of the pressure term but to evaluate the drag of configurations using the supersonic-area-rule formula of Jones. The influence of the pressure term was evaluated for one simple case.

Equation (1) can be written in coefficient form as

$$C_D = \frac{1}{2\pi}\int_0^{2\pi} C_D(\theta)d\theta \qquad (2)$$

where

$$C_D(\theta) = -\frac{1}{2\pi S}\int_0^{l_t}\int_0^{l_t}\left(\frac{d^2A}{dx^2} - \frac{\beta}{2q}\frac{df}{dx}\right)\left(\frac{d^2A}{dx_1^2} - \frac{\beta}{2q}\frac{df}{dx_1}\right)\log(x - x_1)dx\,dx_1 \quad (3)$$

The quantity $C_D(\theta)$ is most readily determined by solving the integral for $C_D(\theta)$ through a Fourier sine series expression for $\frac{dA}{dx}$ following the method of reference 7 if

$$\phi = \cos^{-1}\left(2\frac{x}{l_t} - 1\right)$$

$$a_n = \frac{2}{\pi}\int_0^{\pi}\left(\frac{dA}{dx} - \frac{\beta}{2}\frac{f}{q}\right)\sin n\phi\, d\phi$$

then $C_D(\theta)$ can be written as

$$C_D(\theta) = \frac{\pi}{4S}\Sigma n a_n^2$$

For the computations of this paper, only 24 terms were used in the Fourier sine series expression for $\frac{dA}{dx}$. Thus,

$$C_D(\theta) = \frac{\pi}{4S}\sum_{n=1}^{n=24} n a_n^2$$

BODY DRAG RESULTS

For bodies of revolution, the calculation of the drag is simplified to some extent because the area distributions are identical for all roll angles. However, except for high-fineness-ratio bodies, it is not possible to assume that the frontal projection of the oblique area cut by the Mach plane is the same as the normal area. Figure 2 shows an example of this for two parabolic bodies of revolution having different fineness ratios and shapes. The area-distribution curve slopes were calculated from the expression

$$\frac{dA}{dx} = \frac{2}{\beta^2}\int_{x_l}^{x_u}\frac{(x - x_0)dx}{\sqrt{\beta^2 R^2(x) - (x - x_0)^2}}$$

The derivation of this expression is given in appendix A. It has also been assumed for the calculations (and all succeeding body calculations) that a cylinder can be added at the base of the body without altering the drag. If this were not done, the solution would require the flow to fill the area behind the base which would exceed the limitations of the linearized theory. Figure 2 shows large changes in the peak slope over the afterbody of the fineness-ratio-6.04 configuration; these changes would lead to a significant drag variation with Mach number.

The evaluation of the slope of the oblique area distributions is extremely difficult except for simple bodies. There naturally arises the question as to whether this is worth while if the pressure term is ignored.

As derived in appendix B, the local force acting on the oblique area of a body of revolution is

$$\frac{f}{q} = -\beta A \frac{dC_p}{dx}$$

The only assumption made in derivation of $\frac{f}{q}$ is that $\frac{dC_p}{dx}$ is constant over the oblique area. This is a reasonable assumption except for bodies having discontinuities, and high local slopes. Then,

$$\frac{dA}{dx} - \frac{\beta}{2}\frac{f}{q} = \frac{dA}{dx} + \frac{\beta^2 A}{2}\frac{dC_p}{dx}$$

Thus, the error in the drag introduced by ignoring the pressure term is dependent on the pressure gradient $\frac{dC_p}{dx}$.

It would be expected that the drag for a conical nose with an attached shock wave over which the pressure is constant at zero angle of attack would be least affected by the pressure term. (The pressure term takes on a value only near the juncture with the cylinder; however, the pressure term was not evaluated in this region.) Figure 3 presents a comparison of the drag of various cones calculated with the supersonic-area-rule formula with the exact theory drag of reference 8. The lowest Mach number of the comparison corresponds to the lowest Mach number for entirely supersonic flow on the cone as calculated with the exact theory. The highest Mach number of the comparison was arbitrarily taken as that at which the slope of the Mach line equaled one-half the slope of the nose. The agreement between the two theories is remarkable, within 5 percent except for a few points.

A better comparison may be made by plotting $C_D(l/r_m)^2$ against $\beta r_m/l$, the quantity which defines the frontal projection of the oblique area distribution. This has been done in figure 4 to give drag in dimensionless or collapsed form. The drags from exact theory (5° half angle cone was chosen as representative), slender body theory (ref. 9), and supersonic-area-rule theory are shown. The comparison shows the great improvement of the area-rule theory over the slender-body theory at values of $\beta r_m/l$ greater than 0.2, and the good agreement of the area-rule result with the exact theory to $\beta r_m/l$ of about 0.7. At higher values of $\beta r_m/l$ the area-rule theory is in error, possibly first because the pressure term is neglected but finally, near $\beta r_m/l = 1$, because the assumptions of the linearized theory are violated. At $\beta r_m/l = 1$, the Mach line lies on the cone surface, which corresponds to the realm of hypersonic flows. (See ref. 10.)

For a body with curvature, for example, a nose of parabolic profile, the pressure over the nose is variable, and the influence of the pressure term may be significant. Figure 5 presents the drag for noses of parabolic profile in collapsed form. Here the supersonic-area-rule theory is an improvement over slender-body theory but in only partial agreement with the more exact second-order theory of reference 11. Inclusion of the pressure term, evaluated by using second-order pressure distributions, however, does give agreement with some of the second-order-theory results. Since the second-order-theory drags do not collapse into one curve, agreement should be expected only with those points for which the pressure distribution used in evaluating the pressure term apply. However, this was not the case. For example, the pressure distribution used for the pressure term calculation at $\beta r_m/l = 0.3$ corresponds to the flagged symbol. For the parabolic noses, both the area-rule theory and the area-rule theory plus the pressure correction cannot be expected to apply near and above $\beta r_m/l = 0.5$, where the slope of the Mach line equals the slope of the nose tip.

Figure 6 presents a comparison of the pressure drag from supersonic-area-rule theory with experiment and slender-body theory for a family of parabolic bodies of revolution. The experimental drags were taken from references 12 and 13. In determining the experimental pressure drags, the friction drag was assumed turbulent and evaluated by using the subsonic drag level and the results of reference 14 for the effects of Mach number and Reynolds number; the fin pressure drags were assumed identical and taken from reference 15; and the base drags were small and were subtracted when available. The slender-body-theory drags were calculated using the curves of reference 9.

As would be expected, the comparisons show the increasing ability of both the area-rule theory and slender-body theory to predict the drag as the body fineness ratio is increased. In most cases, the area-rule theory offers a significant improvement over slender-body theory. The area-rule theory and slender-body theory are in agreement near $M = 1$, since at this Mach number the supersonic-area-rule theory reduces to slender-body theory.

From these nose and complete-body comparisons that have been made, the following conclusion can be drawn. The area-rule drag of bodies can be predicted to a greater degree of accuracy by using the frontal projection of oblique areas at a given Mach number than by using normal areas, if, at the Mach number under consideration, the limitations of the linearized theory are not exceeded. This is illustrated by the comparison between the drag at a given Mach number and the drag near $M = 1$ especially for the low-fineness-ratio bodies. It is not to be inferred from the above statement that the supersonic-area-rule method is recommended for evaluating the drags of bodies of revolution. However, when the drags of wing-body combinations for which the body area distribution is needed are determined, the oblique area distribution should be used if the body is of low fineness ratio or has low-fineness-ratio components.

CALCULATION OF WING-BODY DRAG

The difficulty in computing the wave drag of wing-body configurations can be considerably reduced if the configuration meets the following conditions: first, the body is of sufficiently high fineness ratio so that the change in body-area distribution with Mach number is small, and second, the wing is thin. These conditions imply also that the pressure term is negligible. Some feel for the body fineness ratios necessary for the above condition to be met can be obtained from the preceding section on bodies of revolution. The assumption of a thin wing allows the Mach plane intersecting the wing obliquely to be replaced by a plane perpendicular to the wing chord plane intersecting the wing plane along the same line as the Mach plane. Note that, at zero roll angle, the Mach plane is normal to the wing chord plane but is not normal to the wing chord plane at any other roll angle for a Mach number other than $M = 1$. Also the angle between the Mach plane and the normal to the wing chord plane is greatest and equal to $\tan^{-1}\beta$ at a roll angle of 90°.

Appendix C presents a simple analytical method for evaluating wing area distributions and area-distribution-curve slopes. The curves necessary for evaluating these quantities (figs. 16 and 17) are applicable only to 65A series airfoils, but similar curves can be made up for other airfoil sections.

In order to get an idea of the applicability of the thin-wing assumption, a calculation has been made of the true area-distribution-curve-slope variation for 60° delta wing having an NACA 65A006 airfoil section for a roll angle of 90° and a Mach number of 1.414. In order to simplify the calculation, the wing was approximated by a sufficient number of linear-slope elements to define the airfoil section adequately. With this approximation the Mach plane intersection with the wing surface was made up of straight lines. The expression for the frontal projection of the oblique area was then easily evaluated and differentiated to obtain the slope. The results of the calculation are presented in figure 7. Although the slopes for the upper and lower half wings are significantly different, the total slope agrees almost exactly with the slope obtained by using the thin-wing assumption. On the basis of this result, it is felt that the thin-wing solution should be adequate for wings of present-day interest.

For the wing-body combinations of this paper, an additional simplification was allowed in the supersonic-area-rule wave-drag calculations. Since the tail fins mounted on the models were thin and relatively small (see ref. 16), their drags were subtracted as tares. Then, since the bodies for all cases were of high fineness ratio (and identical), the body-area-distribution-curve slopes were considered independent of Mach number, and the changes in the area-distribution-slope curves with Mach number and roll angle were due entirely to the wings. As derived in appendix C, the area distribution for a given wing (m fixed) is dependent only on the value of $\frac{\beta \cos \theta}{\tan \Lambda}$. Thus, the area-distribution-slope curves for the wing-body configuration are dependent only on the value of $\frac{\beta \cos \theta}{\tan \Lambda}$. Then, from equation (2) and because of the symmetry of the configuration,

$$C_D(M) = \frac{2}{\pi}\int_0^{\pi/2} C_D(\theta)d\theta$$

In order to obtain the wave drag of the configuration, a plot of C_D against θ is required. This can be computed if a plot of C_D against $\frac{\beta \cos \theta}{\tan \Lambda}$ is given, since the angle θ is known for fixed values of $\frac{\beta}{\tan \Lambda}$ and $\frac{\beta \cos \theta}{\tan \Lambda}$. The configuration drag is simply the average drag between $\theta = 0$ and $\frac{\pi}{2}$.

For the wing-body calculations of this paper the bodies were identical. The body-area-distribution-slope curves are shown in figure 2(b). The curve for $M = 1.414$ was chosen as representative for the Mach number

range of interest. The wing area distributions and area-distribution-curve slopes were obtained by using methods similar to that given in appendix C. In addition, a limiting value of $\frac{\beta \cos \theta}{\tan \Lambda} = 0.8$ was set for configurations having blunt leading-edge airfoils. (Above $\frac{\beta \cos \theta}{\tan \Lambda} = 1$, the Mach line lies behind the wing leading edge, and the linear theory is no longer valid for blunt airfoils.)

An example of the wave drag calculation for the most extreme configuration investigated (60° delta wing, NACA 65A006 airfoil) is presented in figures 8, 9, and 10. Figure 8 shows nondimensional plots of $\frac{dA}{dx}$ against ϕ for various values of $\frac{\beta \cos \theta}{\tan \Lambda}$. Figure 9 shows the effect on C_D of the number of terms in the series solution. Except at $\frac{\beta \cos \theta}{\tan \Lambda} = 0$ and 0.8, convergence was apparently obtained within 24 terms. Figure 10 shows the variation of the area distribution drag with $\frac{\beta \cos \theta}{\tan \Lambda}$, the variation of area distribution drag with roll angle, and the variation of the configuration drag with $\frac{\beta}{\tan \Lambda}$.

WING-BODY DRAG COMPARISONS

Figure 11 presents some wave-drag comparisons for wing-body combinations. The experimental wing-body results were taken from references 16 to 19. The wing-body wave drags were obtained in the following manner. The friction drags were assumed to be turbulent and were estimated by using the results of reference 14. Base drags and fin pressure drags were subtracted using the results of reference 16. The equivalent-body drags for a Mach number of 1 were obtained experimentally by using the helium-gun technique described in reference 2. These models had four scaled tail fins. The friction drag was assumed to be the subsonic drag level corrected at higher speeds for Reynolds number and Mach number by using the results of reference 14. Base-drag rise and fin-drag rise were not evaluated for the equivalent-body models. These quantities, however, should be small in the Mach number range where comparison is valid. The supersonic-area-rule-theory drags were evaluated by using the method of the preceding section. No attempt was made to evaluate the drag with the pressure term included. The drag coefficients presented in figure 11 are based on total wing area.

The inability of the supersonic-area-rule theory to predict the drag near $M = 1$ is evident for nearly all cases. However, the agreement at the higher Mach numbers between the theoretical drags and the experimental

wing-body drags is excellent and within the accuracy of evaluating the experimental wave drag, except for three configurations. Two of these configurations (figs. 11(c) and 11(g)) had 6-percent-thick wings which were the thickest wings investigated. The third configuration (fig. 11(h)) had a $4\frac{1}{2}$- percent-thick airfoil but with fairly steep wedge components. For these configurations, a significant effect of the neglected pressure term may be possible. As a result, the drags calculated for configurations having wings of these thicknesses and sections should be viewed with caution.

The comparisons in figure 11 show that the equivalent-body drags give a good approximation to the experimental wing-body drags up to a Mach number of 1, except for the two configurations having 6-percent-thick wings (figs. 11(c) and 11(g)). This result is in agreement with reference 2 which shows the validity of the transonic-area rule decreases with increasing wing-thickness ratio. At Mach numbers above 1, the agreement is variable but tends to be consistent with the flatness of the corresponding theoretical curve. That is, as the theoretical drag variation with Mach number becomes smaller, the equivalent body gives a better approximation of the supersonic-drag level. This would be expected, since a flat theoretical curve indicates that the variation in area-distribution drag with roll angle or Mach number is small. Then the drag for the Mach number 1 or roll angle 90° area distribution (corresponding to the equivalent body) is representative of the configuration drag.

Figure 12 shows the comparison between experimental-configuration drag and equivalent-body drag for an airplane configuration. The comparison shows an extreme example, compared with the relatively good results of reference 2, of the inability of the equivalent body to predict the supersonic-drag level. The equivalent-body drag is approximately 40 percent low in spite of the low aspect ratio of the configuration. Apparently, the configuration tail surfaces cause the area distribution to change markedly at low supersonic speeds. Below $M = 1$, the equivalent body gives a fair representation of the configuration drag. The drag of the configuration minus the tail surfaces could probably be calculated to the degree of accuracy shown in figure 11. The influence of the tail surfaces, however, may be difficult to evaluate. If the horizontal tail supports a load when the configuration is at zero lift, the influence of the pressure term may be significant. Although no supersonic-area-rule drag calculations were made for this airplane, reference 20 indicates that generally good predictions of complete-airplane drag can be made.[1]

---

[1]Subsequent to the preparation of this paper, NACA RM A56I07 has been prepared at the Ames Laboratory and presents supersonic-area-rule calculations for a configuration similar to the one shown in figure 12 but with small differences in area distribution in addition to the absence of a canopy.

EVALUATION OF COMPONENT AND INTERFERENCE DRAGS

As was shown in the preceding section, the supersonic area rule can be a useful tool in evaluating the supersonic drag of a wing-body configuration. In order to assess the efficiency of the combination as a whole, however, the effects of the combination on the component drags and the interference drag between the components must be known. The supersonic area rule provides a valuable method for evaluating these effects.

The supersonic-area-rule equation can, of course, be used in evaluating the drags of individual wing and body components. This was done for a number of bodies in a previous section of this paper. The same can be done for isolated wings. An example of this is shown in figure 13 where the drag of delta wings having 65A series sections is plotted in collapsed form. The area-rule result is compared with a result obtained by the method of Beane (ref. 21). The two methods are just two forms of the same linearized wing theory. The agreement between the two methods is good.

An example of the effect of the wing-body configuration on wing drag is presented in figure 14. The calculation is for the configuration having the closest agreement between the theoretical and experimental drags (fig. 11(b)). In this figure, the drag of the exposed-wing panels based on total and exposed wing areas is compared with the isolated wing drag. Separation of the wing panels gives approximately a 10-percent reduction in wing drag coefficient at Mach numbers above 1.3. As the Mach number approaches 1, this favorable effect disappears. This would be expected, for at $M = 1$ the area distributions of the exposed wing panels and the isolated wing would be identical if the body were cylindrical.

Figure 15 shows an evaluation of the interference drag for the same configuration. The sum of the calculated body and wing drags is compared with the calculated configuration drag. The curves show a favorable interference effect at Mach numbers below $M = 1.3$. At Mach numbers above 1.3, interference drag is, for all practical purposes, zero. Thus for this configuration, at Mach numbers greater than 1.3, the only beneficial effect of combining the wing with the body comes from the separation of the wing panels.

CONCLUSIONS

An investigation has been made of abilities of the equivalent-body technique and a 24-term Fourier series application of the supersonic-area-rule method to predict wave drag at transonic and supersonic speeds. From the theoretical and experimental comparisons made, the following conclusions can be drawn:

1. The area-rule drag of the bodies of revolution presented in this report are predicted to a greater degree of accuracy by using the frontal projection of oblique areas at a given Mach number than by using normal areas.

2. The supersonic wave drag of slender-wing—body configurations can be predicted with the supersonic-area-rule formula. For the wing-body configurations investigated, the best agreement was obtained for the configurations employing the thinnest wings.

3. The equivalent body technique provides a good method for predicting the wave drag of certain wing-body combinations at and below Mach number 1. At Mach numbers above 1, the equivalent body wave drags can be misleading.

Langley Aeronautical Laboratory,
National Advisory Committee for Aeronautics,
Langley Field, Va., April 6, 1956.

APPENDIX A

AREA DISTRIBUTION SLOPE FOR BODIES OF REVOLUTION CUT BY OBLIQUE MACH PLANES

The area distributions are identical for all roll angles. For simplicity a roll angle of 90° will be used in the derivation.

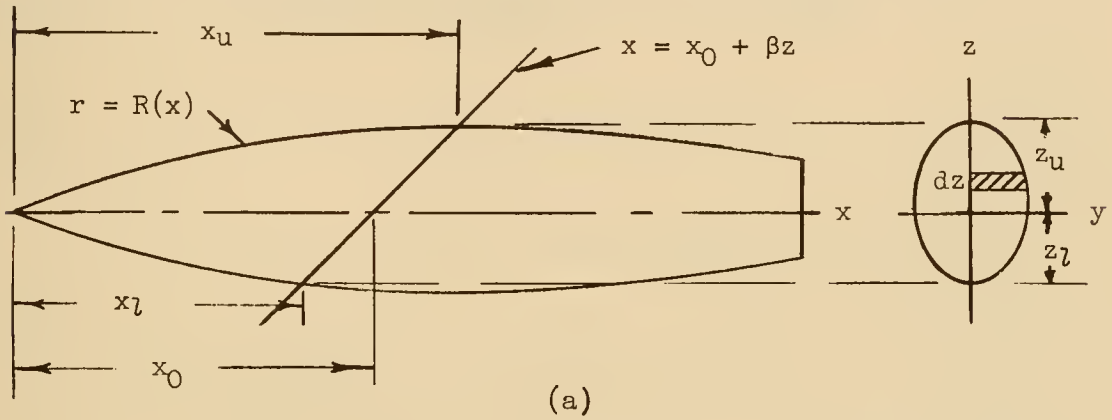

(a)

The frontal projection of the oblique area cut by the Mach plane (see sketch (a)) is given by the equation:

$$A = 2\int_{z_l}^{z_u} y\, dz$$

From the equation for the Mach plane, z is related to x by

$$z = \frac{x - x_0}{\beta}$$

and

$$dz = \frac{1}{\beta}\, dx$$

The equation relating y and x is given by

$$y = \sqrt{R^2(x) - z^2} = \sqrt{R^2(x) - \frac{(x - x_0)^2}{\beta^2}} = \frac{1}{\beta}\sqrt{\beta^2 R^2(x) - (x - x_0)^2} \qquad (A1)$$

Then,

$$A = \frac{2}{\beta^2} \int_{x_l}^{x_u} \sqrt{\beta^2 R^2(x) - (x - x_0)^2}\, dx \tag{A2}$$

Differentiating the expression for A gives

$$\frac{dA}{dx_0} = \frac{2}{\beta^2} \int_{x_l}^{x_u} \frac{(x - x_0)}{\sqrt{\beta^2 R^2(x) - (x - x_0)^2}}\, dx \tag{A3}$$

where x_l and x_u are the roots of $x = x_0 - \beta R(x)$ and $x = x_0 + \beta R(x)$, respectively.

APPENDIX B

THE NET FORCE ACTING ON THE OBLIQUE AREA OF A BODY OF REVOLUTION AT ZERO ANGLE OF ATTACK

For a body of revolution at zero angle of attack, the net force is independent of roll angle. The derivation will be made for a roll angle of 90°.

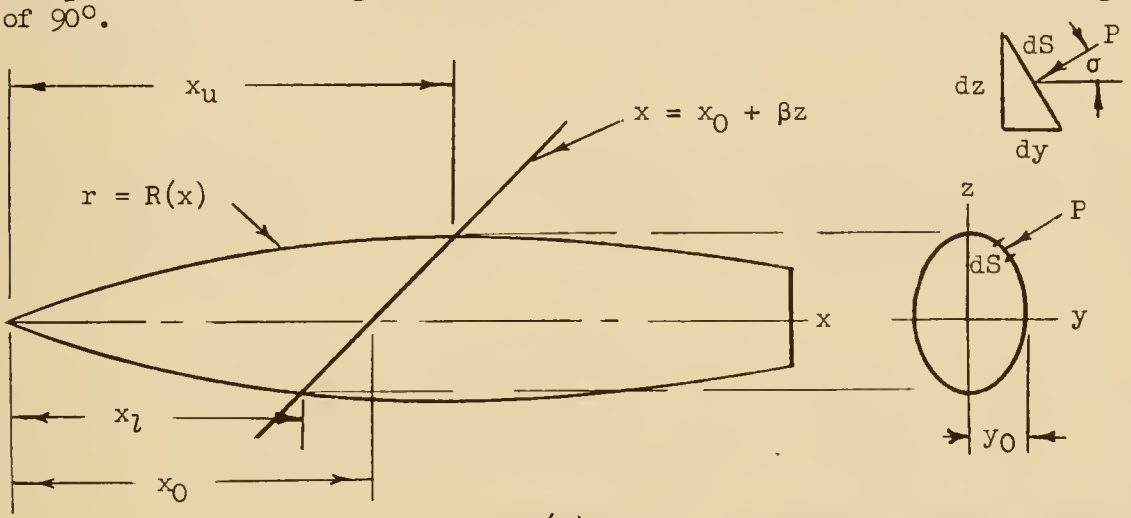

(b)

The net force in the θ direction (the z-direction for a roll angle of 90°) (see sketch (b)) can be written as

$$\frac{f}{q} = -\int_C C_p \sin\sigma \, dS$$

Since $dS = \sqrt{dy^2 + dz^2}$ and $\sin\sigma = \frac{dy}{\sqrt{dy^2 + dz^2}}$,

$$\frac{f}{q} = \int_C C_p \, dy$$

The pressure coefficient at zero lift is a function of x only. The equation for y in terms of x is given by equation (1) of appendix A as follows:

$$y = \frac{1}{\beta}\sqrt{\beta^2 R^2(x) - (x - x_0)^2}$$

and

$$dy = \frac{\beta^2 R(x)\frac{dr}{dx} - (x - x_0)}{\beta\sqrt{\beta^2 R^2(x) - (x - x_0)^2}}\,dx$$

Then, the net force can be written as

$$\frac{f}{q} = \left(-2\int_0^{y_0} C_p\,dy\right)_{\text{upper surface}} + \left(2\int_0^{y_0} C_p\,dy\right)_{\text{lower surface}}$$

$$\frac{f}{q} = -\frac{2}{\beta}\int_{x_u}^{x_0} \frac{C_p\left[\beta^2 R(x)\frac{dr}{dx} - (x - x_0)\right]}{\sqrt{\beta^2 R^2(x) - (x - x_0)^2}}\,dx + \frac{2}{\beta}\int_{x_l}^{x_0} \frac{C_p\left[\beta^2 R(x)\frac{dr}{dx} - (x - x_0)\right]}{\sqrt{\beta^2 R^2(x) - (x - x_0)^2}}\,dx$$

$$\frac{f}{q} = \frac{2}{\beta}\int_{x_l}^{x_u} \frac{C_p\left[\beta^2 R(x)\frac{dr}{dx} - (x - x_0)\right]}{\sqrt{\beta^2 R^2(x) - (x - x_0)^2}}\,dx$$

Integrating the expression by parts gives

$$\frac{f}{q} = -\frac{2}{\beta}\int_{x_l}^{x_u} \frac{dC_p}{dx}\sqrt{\beta^2 R^2(x) - (x - x_0)^2}\,dx$$

If $\frac{dC_p}{dx}$ is essentially constant between the limits of integrations,

$$\frac{f}{q} = -\frac{2}{\beta}\frac{dC_p}{dx}\int_{x_l}^{x_u} \sqrt{\beta^2 R^2(x) - (x - x_0)^2}\,dx$$

Then, from equation for the frontal projection of the oblique area in appendix A (eq. (A2))

$$\frac{f}{q} = -\beta A\frac{dC_p}{dx}$$

APPENDIX C

METHOD FOR DETERMINING WING-AREA DISTRIBUTION AND AREA-DISTRIBUTION-CURVE SLOPE

This method assumes that the wing is thin and that the oblique Mach plane can be replaced by a plane perpendicular to the wing chord plane. The method also assumes the wing has straight leading and trailing edges and constant thickness ratio.

The method is developed first for pointed-tip wings. Then, corrections are made for curved-wing—body junctures and finite wing tips. In addition, the right- and left-hand wing panels are considered separately.

Pointed-tip wings.- Consider the right-wing panel shown in the following sketch:

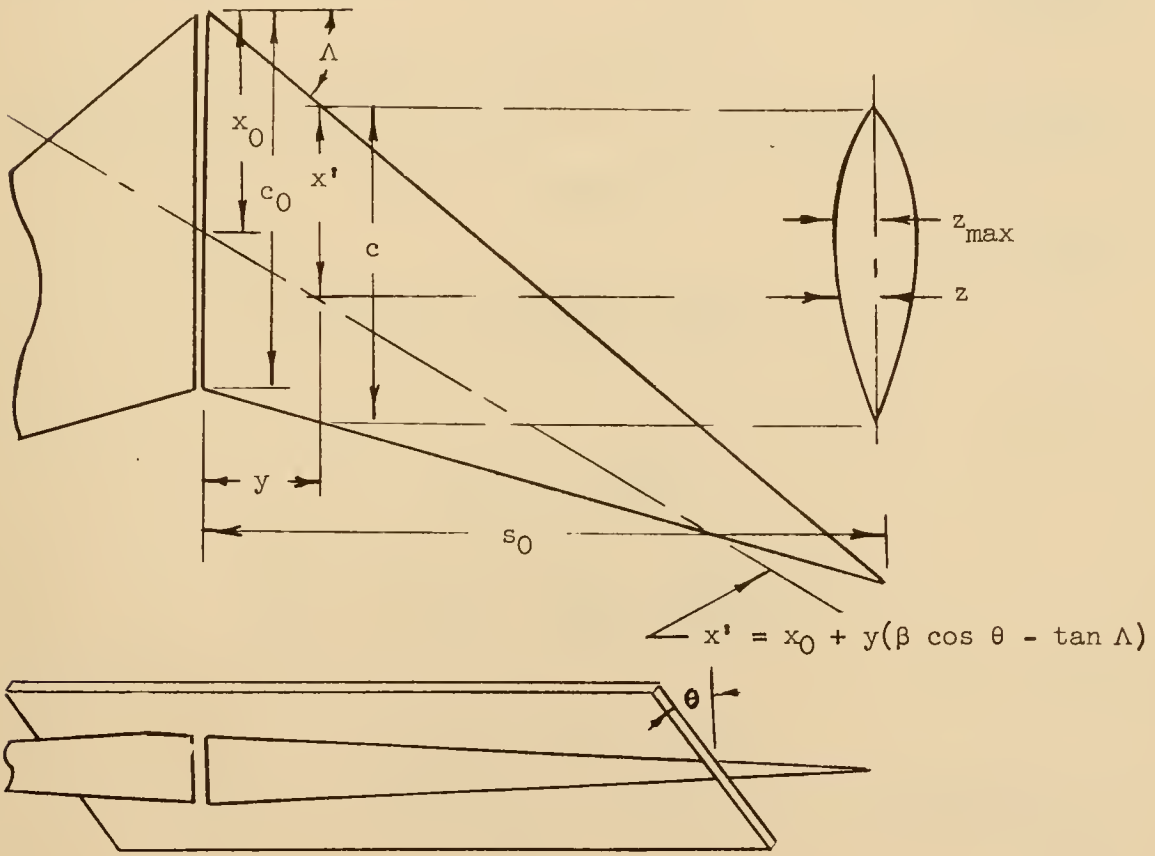

The frontal projection of the area of one wing panel cut by the Mach plane is given by

$$A = 2\int z\, dy$$

and $\frac{z}{c}$ can be written as

$$\frac{z}{c} = \frac{z_{max}}{c}\frac{z}{z_{max}} = \frac{1}{2}\frac{t}{c}f(\nu)$$

Then, for $\frac{t}{c}$ constant,

$$A = s_0 c_0 \frac{t}{c}\int f(\nu)\frac{c}{c_0}\, d\eta$$

The value of η and ν are related by the intersection line of the Mach plane and the wing chord plane for the right-wing panel given by the equation

$$x' = x_0 + y(\beta \cos\theta - \tan\Lambda)$$

and for the left-wing panel by the equation

$$x' = x_0 + y(\beta \cos\theta + \tan\Lambda)$$

Then,

$$\nu = \frac{c_0}{c}\left[\nu_0 + \frac{s_0}{c_0}(\beta \cos\theta \pm \tan\Lambda)\eta\right]$$

With

$$\frac{c}{c_0} = 1 - \eta$$

$$\nu = \frac{1}{1-\eta}\left[\nu_0 + \frac{s_0}{c_0}(\beta \cos\theta \pm \tan\Lambda)\eta\right]$$

and

$$\eta = \frac{\nu_0 - \nu}{(\tan\Lambda \pm \beta \cos\theta)\frac{s_0}{c_0} - \nu}$$

Let

$$m = \frac{s_0}{c_0}\tan\Lambda$$

In terms of tapered wing geometry, m is given by

$$m = \frac{A}{4}\frac{1 + \lambda}{1 - \lambda}\tan \Lambda$$

Then,

$$\eta = \frac{\nu_0 - \nu}{m\left(1 \pm \frac{\beta \cos \theta}{\tan \Lambda}\right) - \nu}$$

Let

$$K = m\left(1 + \frac{\beta \cos \theta}{\tan \Lambda}\right)$$

for the left-wing panel and

$$K = m\left(1 - \frac{\beta \cos \theta}{\tan \Lambda}\right)$$

for the right-wing panel. Then,

$$\eta = \frac{\nu_0 - \nu}{K - \nu}$$

$$\frac{d\eta}{d\nu} = -\frac{K - \nu_0}{(K - \nu)^2}$$

$$\frac{c}{c_0} = 1 - \eta = \frac{K - \nu_0}{K - \nu}$$

$$\frac{c}{c_0}\, d\eta = -\frac{(K - \nu_0)^2}{(K - \nu)^3}\, d\nu$$

The equation for the area can then be written as

$$A = -s_0 c_0 \frac{t}{c}(K - \nu_0)^2 \int_{\nu_{lower}}^{\nu_{upper}} \frac{f(\nu)}{(K - \nu)^3}\, d\nu = s_0 c_0 \frac{t}{c} G(K, \nu_0)$$

The slope of the area-distribution curve is obtained by differentiating the expression for A

$$\frac{dA}{d\nu_0} = s_0 c_0 \frac{t}{c}\left[2(K - \nu_0)\int_{\nu_{lower}}^{\nu_{upper}} \frac{f(\nu)}{(K - \nu)^3}\, d\nu + \frac{(K - \nu_0)^2}{(K - \nu_{lower})^3}\frac{d\nu_{lower}}{d\nu_0} f(\nu_{lower}) - \frac{(K - \nu_0)^2}{(K - \nu_{upper})^3}\frac{d\nu_{upper}}{d\nu_0} f(\nu_{upper})\right]$$

or

$$\frac{dA}{d\nu_0} = s_0 c_0 \frac{t}{c} H(K, \nu_0)$$

Curves of $G(K,\nu_0)$ and $H(K,\nu_0)$ have been made up for a 65A series airfoil and are given in figures 16 and 17 for values of K from 0 to 2.4 and ν_0 from 0 to 1. In evaluating $\int \frac{f(\nu)}{(K - \nu)^3}\, d\nu$, $f(\nu)$ was assumed to vary linearly between airfoil ordinate stations. Figure 18 gives a plot of $f(\nu)$ for this assumption.

For K and ν_0 greater than 1, $G(K,\nu_0)$ and $H(K,\nu_0)$ are given by the expressions

$$G(K,\nu_0) = G(K,1)\frac{(K - \nu_0)^2}{(K - 1)^2}$$

$$H(K,\nu_0) = H(K,1)\frac{(K - \nu_0)}{(K - 1)}$$

For K and ν_0 less than 0, $G(K,\nu_0)$ and $H(K,\nu_0)$ are given by the expressions

$$G(K,\nu_0) = G(K,0)\frac{(K - \nu_0)^2}{K^2}$$

$$H(K,\nu_0) = H(k,0)\frac{(K - \nu_0)}{K}$$

Correction for curved-wing—body juncture.- The following sketch shows a pointed-tip wing mounted on a curved body.

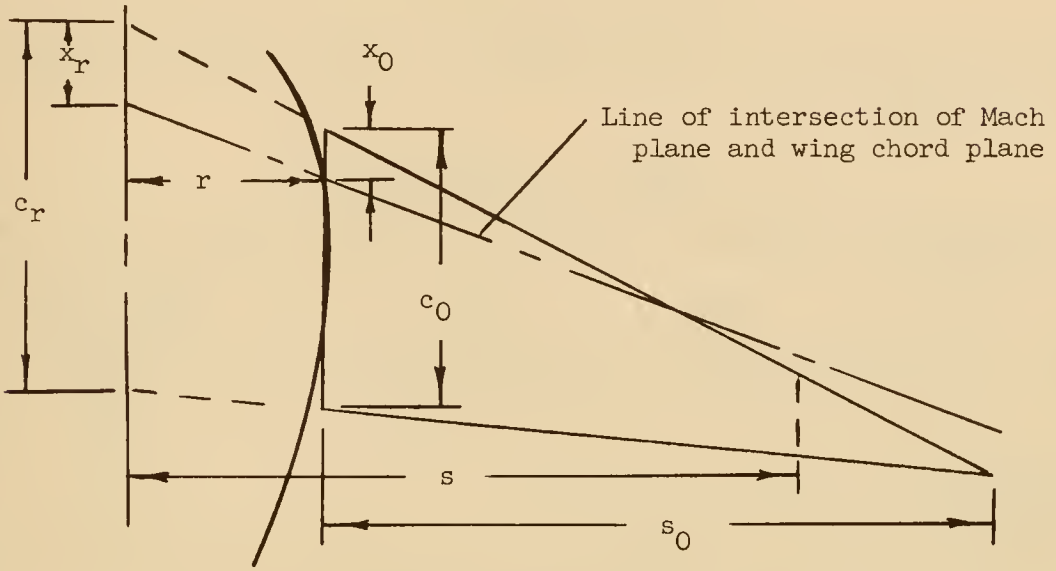

(d)

The areas and slopes will be referred to the actual wing geometry (c_r, s, and λ). The areas and slopes, however, will be for the exposed pointed-wing tip.

In sketch (d) consider one point of intersection of the wing panel with the body. The area of the wing cut by the Mach plane through this point is determined only by the product of s_0c_0 of the exposed wing through the point and the value of ν_0 for the exposed wing at the point of intersection. As the point of intersection changes, s_0, c_0, and ν_0 change and account for the intersection line. Expressed in terms of the actual wing-body characteristics, s_0c_0 is given by

$$s_0c_0 = \frac{c_r s}{1 - \lambda}\left[1 - (1 - \lambda)\frac{r}{s}\right]^2$$

The quantity $\frac{r}{s}$ is related to ν_0 by the expression

$$\nu_0 = \frac{\nu_r - (1 - \lambda)m\frac{r}{s}}{1 - (1 - \lambda)\frac{r}{s}}$$

The area of the exposed wing panel cut by the Mach plane can be written as

$$A = \frac{c_r s \frac{t}{c}}{1 - \lambda}\left[1 - (1 - \lambda)\frac{r}{s}\right]^2 G(K, \nu_0)$$

The area is calculated for given value of ν_0. The center-line value of ν is given by

$$\nu_r = \nu_0\left[1 - (1 - \lambda)\frac{r}{s}\right] + K(1 - \lambda)\frac{r}{s}$$

The slope is obtained by differentiating the expression for A and is given by

$$\frac{dA}{d\nu_r} = \frac{c_r s \frac{t}{c}\left[1 - (1 - \lambda)\frac{r}{s}\right]}{1 - \lambda}\left\{\frac{\left[1 - (1 - \lambda)\frac{r}{s}\right]H(K, \nu_0) - 2(1 - \lambda)\frac{d\frac{r}{s}}{d\nu_0}G(K, \nu_0)}{1 - (1 - \lambda)\frac{r}{s} + (K - \nu_0)(1 - \lambda)\frac{d\frac{r}{s}}{d\nu_0}}\right\}$$

If $\frac{d\frac{r}{s}}{d\nu_0} = 0$,

$$\frac{dA}{d\nu_r} = \frac{c_r s \frac{t}{c}}{1 - \lambda}\left[1 - (1 - \lambda)\frac{r}{s}\right]H(K, \nu_0)$$

Correction for finite wing tip.- In order to correct the pointed-tip wing panel and slopes for the finite wing tip, the areas and slopes outboard of the wing tip are subtracted.

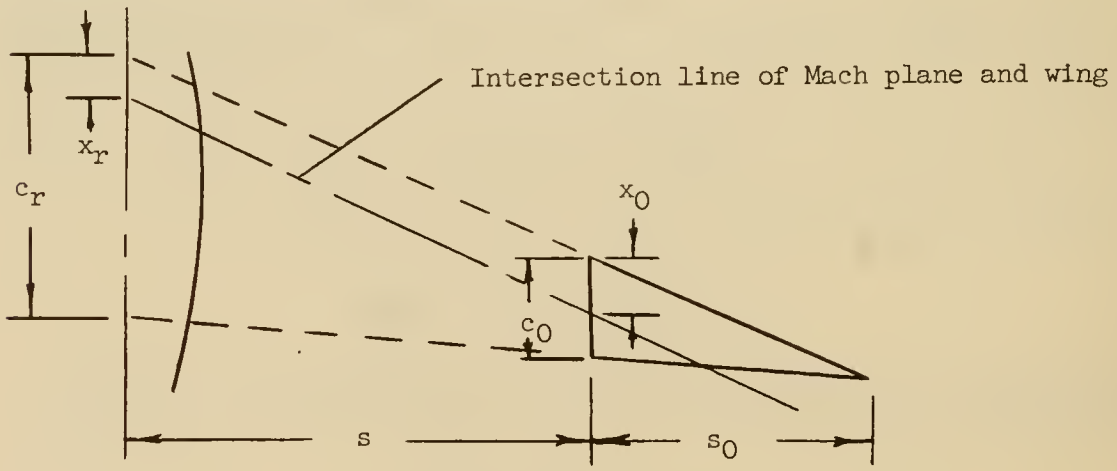

(e)

From sketch (e):

$$s_0 c_0 = c_r s \frac{\lambda^2}{1 - \lambda}$$

Then the areas and slopes are given by

$$A_{tip} = \frac{c_r s \frac{t}{c} \lambda^2}{1 - \lambda} G(K, \nu_0)$$

$$\frac{dA_{tip}}{d\nu_r} = \frac{c_r s \frac{t}{c} \lambda}{1 - \lambda} H(K, \nu_0)$$

The center-line value of ν is given by

$$\nu_r = \nu_0 \lambda + K(1 - \lambda)$$

REFERENCES

1. Whitcomb, Richard T.: A Study of the Zero-Lift Drag-Rise Characteristics of Wing-Body Combinations Near the Speed of Sound. NACA RM L52H08, 1952.

2. Hall, James Rudyard: Comparison of Free-Flight Measurements of the Zero-Lift Drag Rise of Six Airplane Configurations and Their Equivalent Bodies of Revolution at Transonic Speeds. NACA RM L53J21a, 1954.

3. Jones, Robert T.: Theory of Wing-Body Drag at Supersonic Speeds. NACA RM A53H18a, 1953.

4. Holdaway, George H.: Comparison of Theoretical and Experimental Zero-Lift Drag-Rise Characteristics of Wing-Body-Tail Combinations Near the Speed of Sound. NACA RM A53H17, 1953.

5. Alksne, Alberta: A Comparison of Two Methods for Computing the Wave Drag of Wing-Body Combinations. NACA RM A55A06a, 1955.

6. Lomax, Harvard: The Wave Drag of Arbitrary Configurations in Linearized Flow As Determined by Areas and Forces in Oblique Planes. NACA RM A55A18, 1955.

7. Sears, William R.: On Projectiles of Minimum Wave Drag. Quarterly Appl. Math., vol. IV, no. 4, Jan. 1947, pp. 361-366.

8. Staff of the Computing Section, Center of Analysis (Under Direction of Zdeněk Kopal): Tables of Supersonic Flow Around Cones. Tech. Rep. No. 1, M.I.T., 1947.

9. Fraenkel, L. E.: The Theoretical Wave Drag of Some Bodies of Revolution. Rep. No. Aero. 2420, British R.A.E., May 1951.

10. Van Dyke, Milton D.: Application of Hypersonic Small-Disturbance Theory. Jour. Aero. Sci., vol. 21, no. 3, Mar. 1954, pp. 179-186.

11. Van Dyke, Milton D.: Practical Calculation of Second-Order Supersonic Flow Past Nonlifting Bodies of Revolution. NACA TN 2744, 1952.

12. Hart, Roger G., and Katz, Ellis R.: Flight Investigations at High-Subsonic, Transonic, and Supersonic Speeds To Determine Zero-Lift Drag of Fin-Stabilized Bodies of Revolution Having Fineness Ratios of 12.5, 8.91, and 6.04 and Varying Positions of Maximum Diameter. NACA RM L9I30, 1949.

13. Wallskog, Harvey A., and Hart, Roger G.: Investigation of the Drag of Blunt-Nosed Bodies of Revolution in Free Flight at Mach Numbers From 0.6 to 2.3. NACA RM L53D14a, 1953.

14. Chapman, Dean R., and Kester, Robert H.: Turbulent Boundary-Layer and Skin-Friction Measurements in Axial Flow Along Cylinders at Mach Numbers Between 0.5 and 3.6. NACA TN 3097, 1954.

15. Stevens, Joseph E., and Purser, Paul E.: Flight Measurements of the Transonic Drag of Models of Several Isolated External Stores and Nacelles. NACA RM L54L07, 1955.

16. Morrow, John D., and Nelson, Robert L.: Large-Scale Flight Measurements of Zero-Lift Drag of 10 Wing-Body Configurations at Mach Numbers From 0.8 to 1.6. NACA RM L52D18a, 1953.

17. Wallskog, Harvey A., and Morrow, John D.: Large-Scale Flight Measurements of Zero-Lift Drag and Low-Lift Longitudinal Characteristics of a Diamond-Wing—Body Combination at Mach Numbers From 0.725 to 1.54. NACA RM L53C17, 1953.

18. Welsh, Clement J., Wallskog, Harvey A., and Sandahl, Carl A.: Effects of Some Leading-Edge Modifications, Section and Plan-Form Variations, and Vertical Position on Low-Lift Wing Drag at Transonic and Supersonic Speeds. NACA RM L54K01, 1955.

19. Sandahl, Carl A., and Stoney, William E.: Effect of Some Section Modifications and Protuberances on the Zero-Lift Drag of Delta Wings at Transonic and Supersonic Speeds. NACA RM L53L24a, 1954.

20. Holdaway, George H., and Mersman, William A.: Application of Tchebichef Form of Harmonic Analysis to the Calculation of Zero-Lift Wave Drag of Wing-Body-Tail Combinations. NACA RM A55J28, 1956.

21. Beane, Beverly: The Characteristics of Supersonic Wings Having Biconvex Sections. Jour. Aero. Sci., vol. 18, no. 1, Jan. 1951, pp. 7-20.

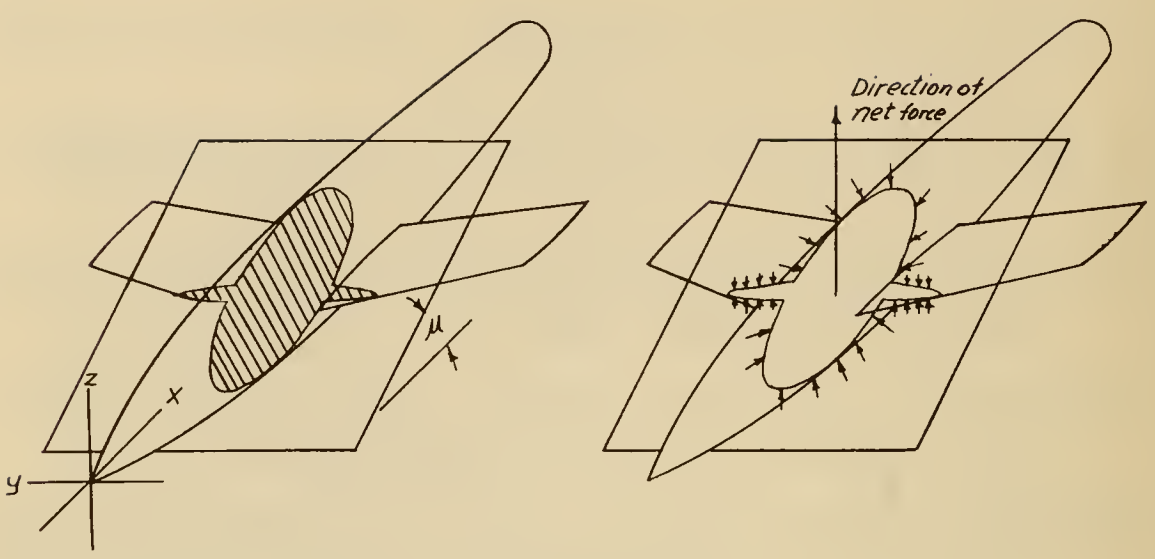

(a) $\theta = 90^{\circ}$.

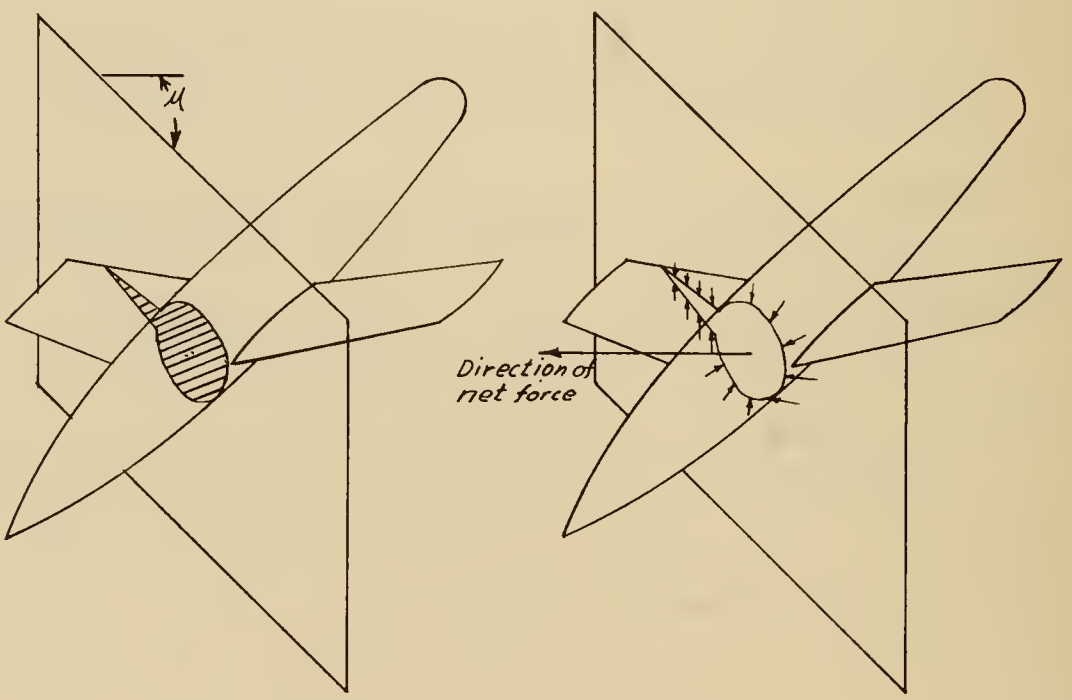

(b) $\theta = 0^{\circ}$.

Figure 1.- The areas and pressures which influence the drag of configurations at supersonic speeds.

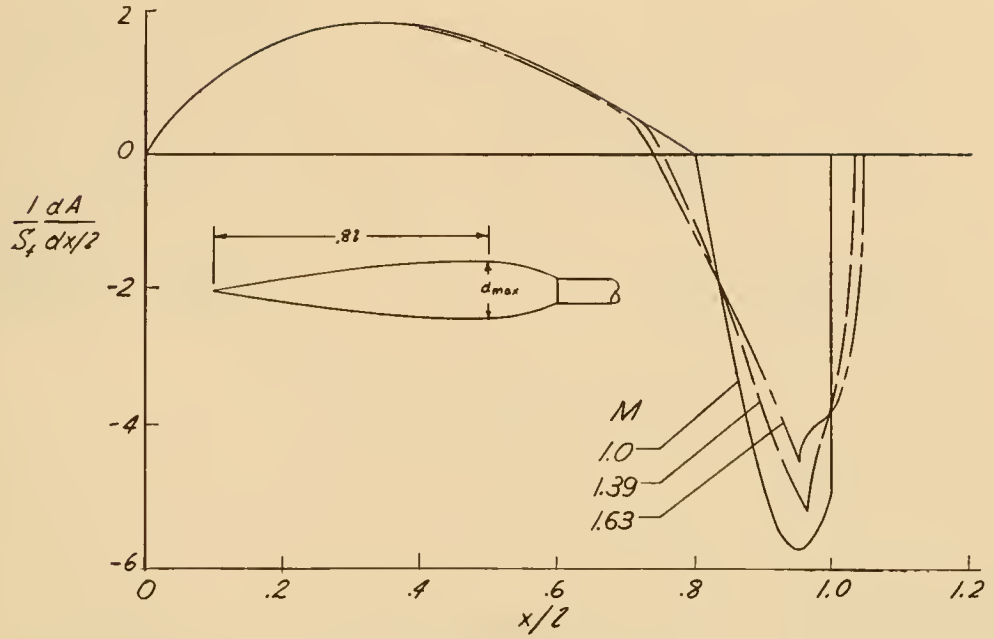

(a) Low-fineness-ratio body; $\frac{l}{d} = 6.04$.

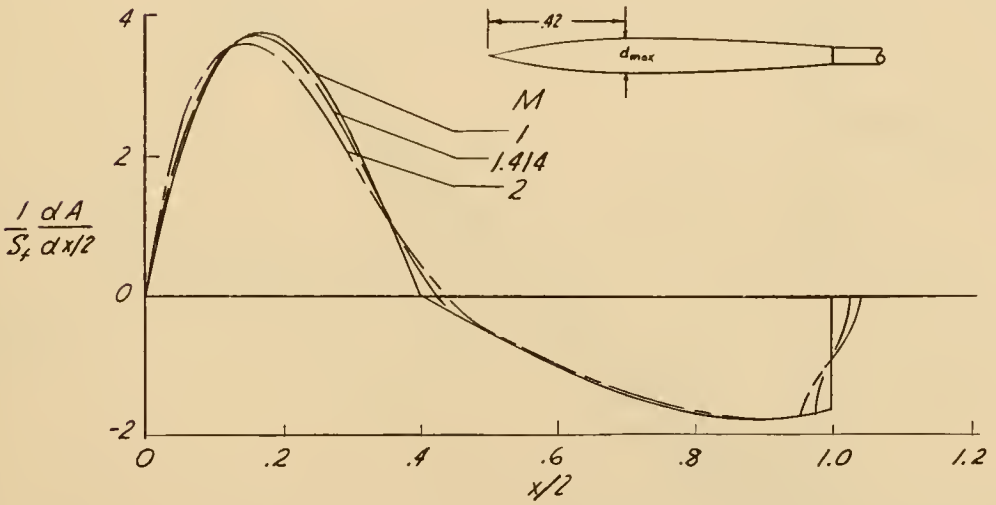

(b) High-fineness-ratio body; $\frac{l}{d} = 10$.

Figure 2.- The effect of Mach number on the area-distribution-curve slope of bodies of revolution.

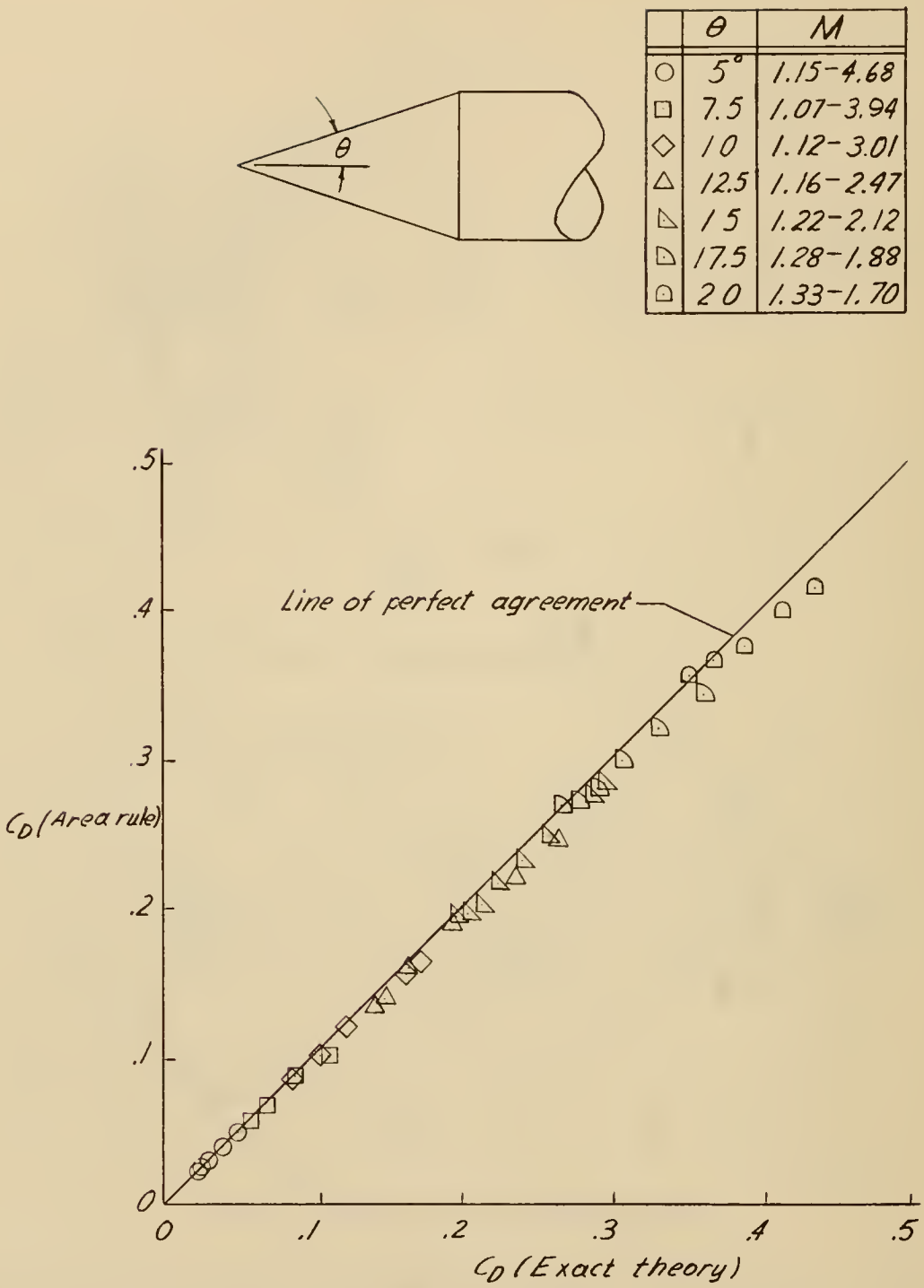

Figure 3.- Comparison of the drag of cones calculated with the area rule with the drag from exact theory (ref. 8).

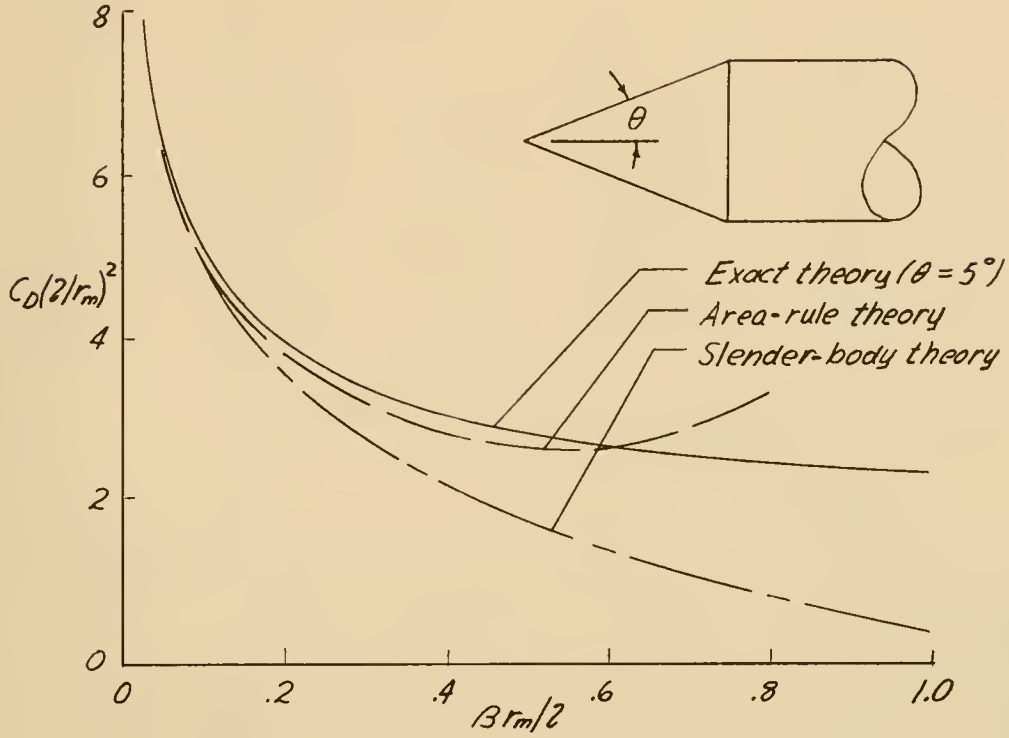

Figure 4.- The drag of cones in collapsed form.

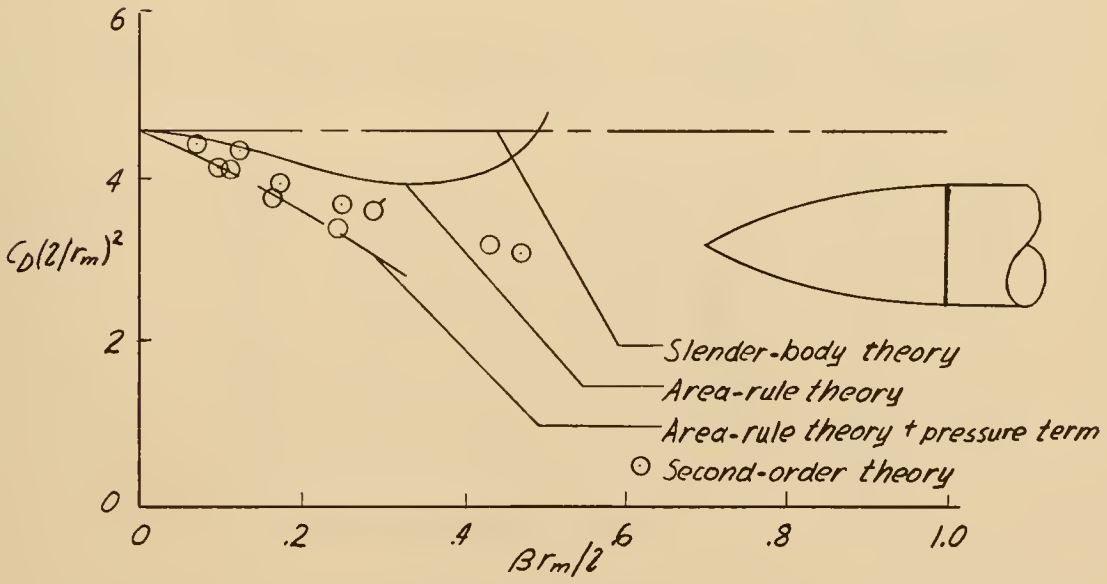

Figure 5.- The drag of parabolic noses in collapsed form.

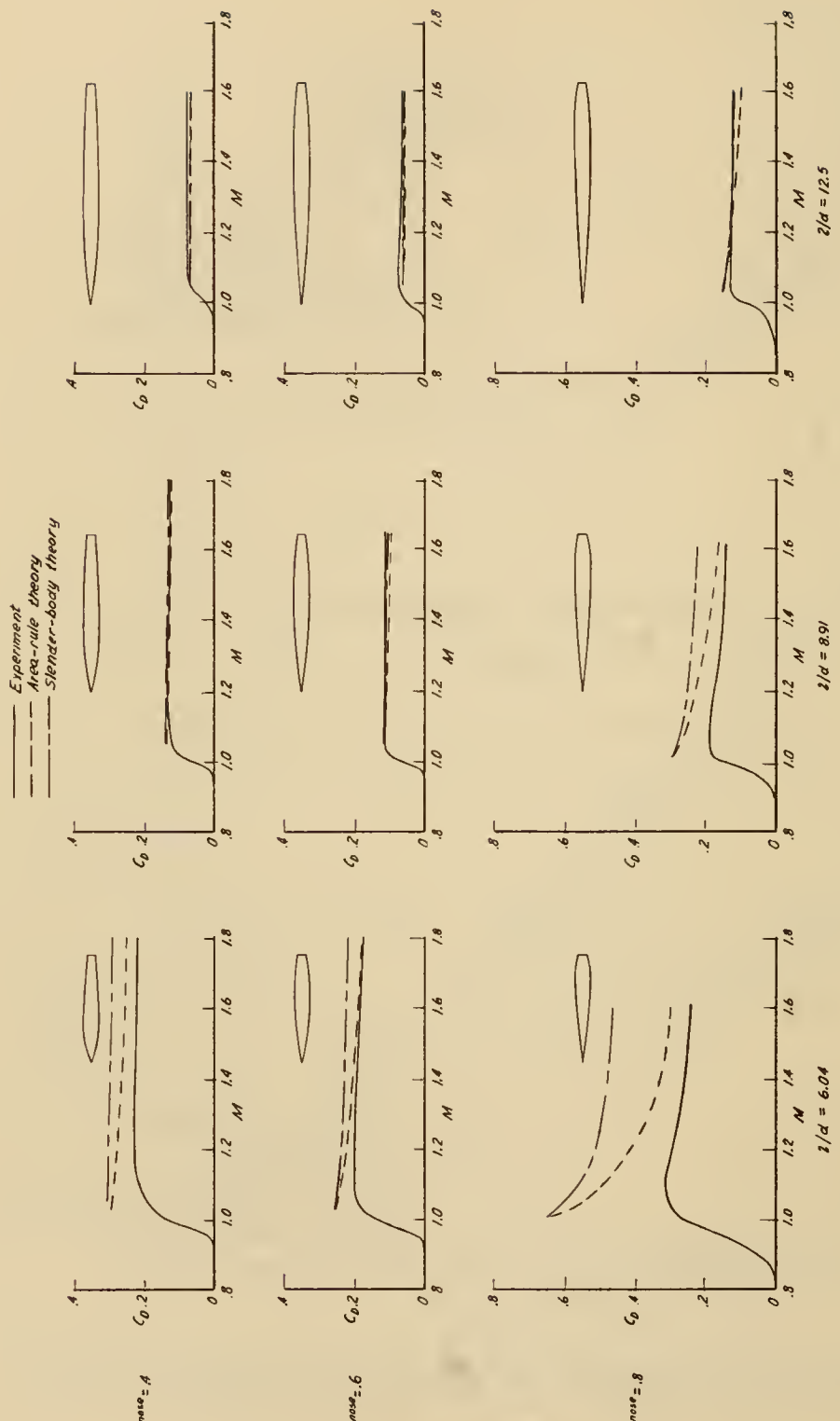

(a) $\frac{l_n}{l}$ = 0.4, 0.6, and 0.8.

Figure 6.- Comparison of the drag of parabolic bodies calculated with the area rule with experiment and slender-body theory.

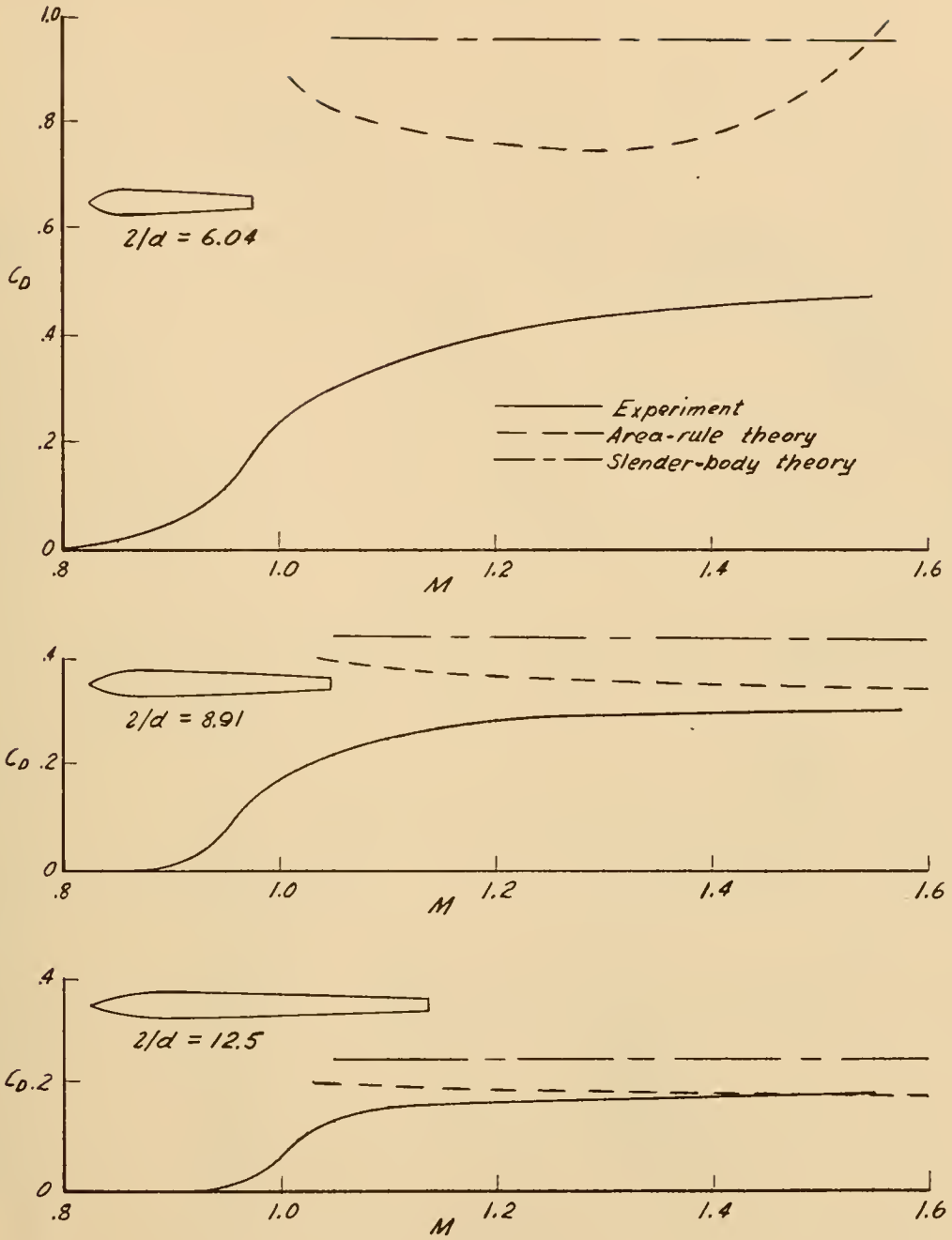

(b) $\frac{l_{nose}}{l} = 0.2$.

Figure 6.- Concluded.

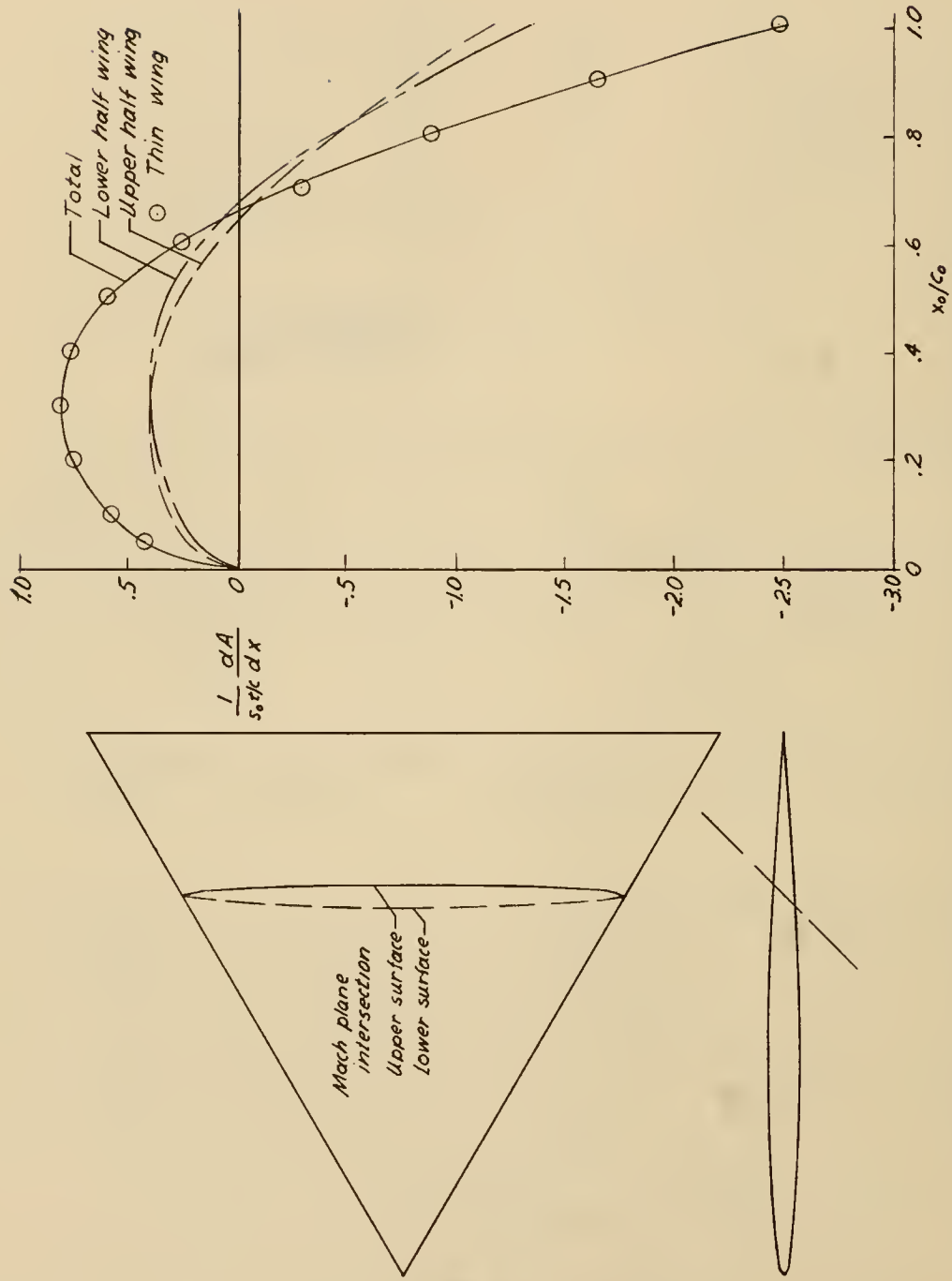

Figure 7.- Comparison of the area-distribution-curve slopes for a delta wing obtained by using the thin- and thick-wing assumptions. NACA 65A006 airfoil section; M = 1.414; $\theta = 90^{\circ}$.

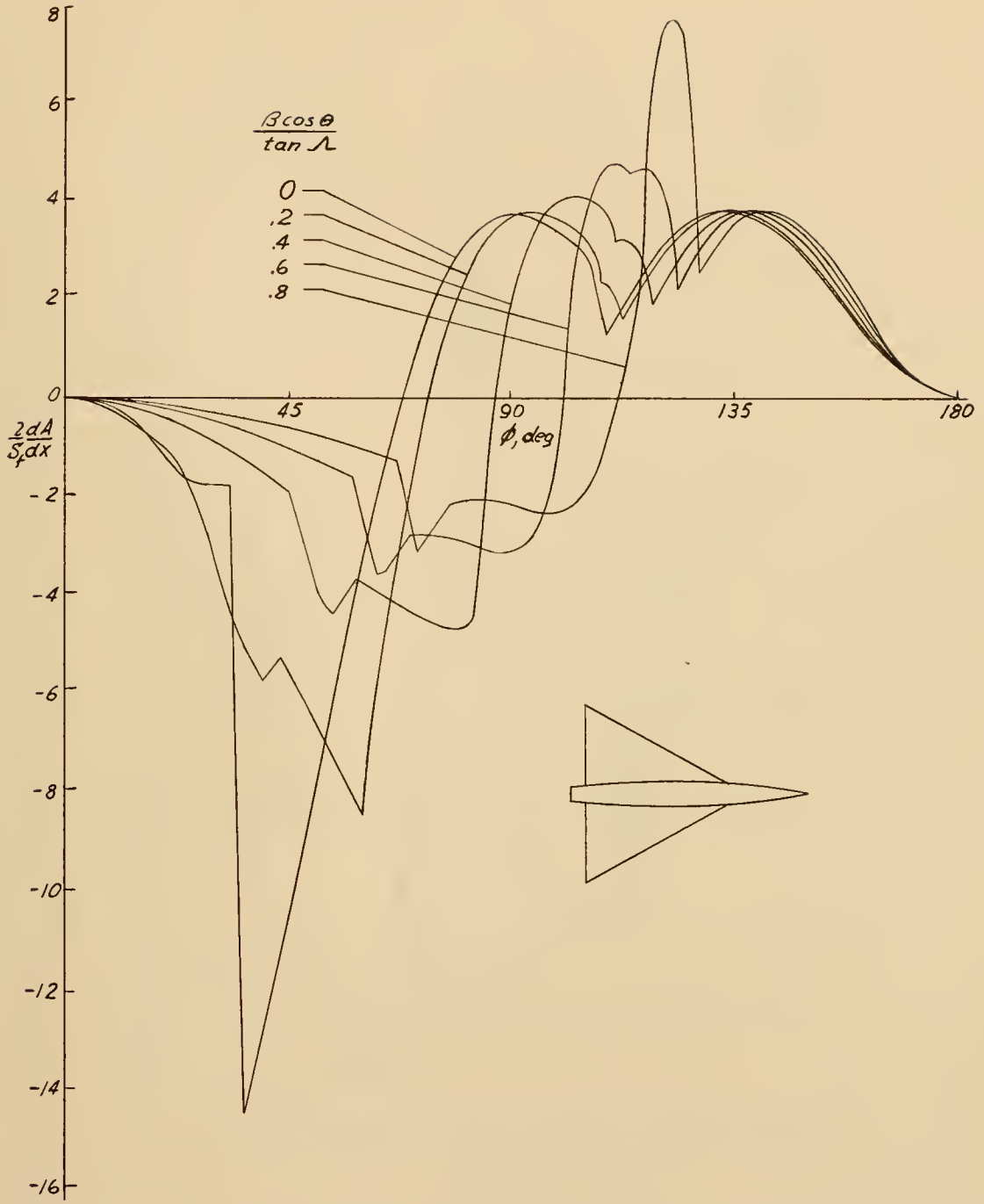

Figure 8.- Example of the area-distribution-curve slope for a wing-body configuration for various values of $\beta \cos \theta / \tan \Lambda$. 60° delta wing; NACA 65A006 airfoil section.

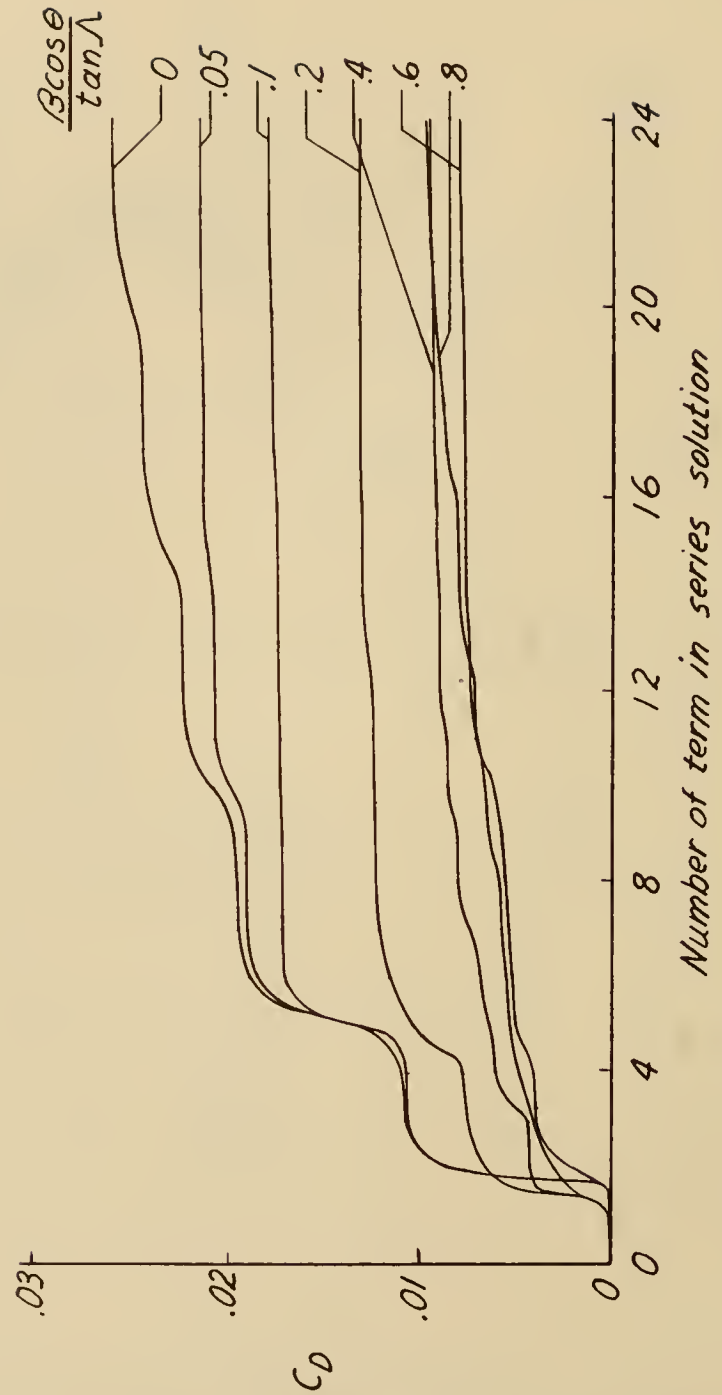

Figure 9.- Effect of the number of terms on the convergence of the series expression for the drag. 60° delta wing; NACA 65A006 airfoil section.

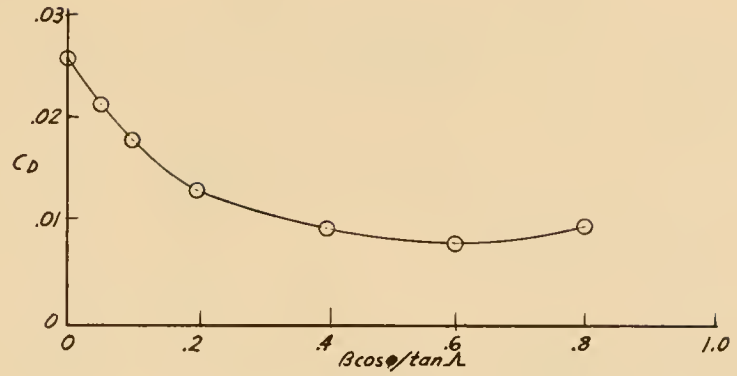

(a) Area distribution drag.

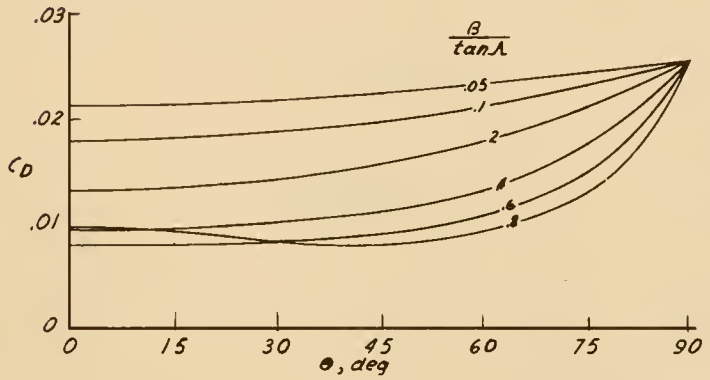

(b) Area distribution drag against roll angle.

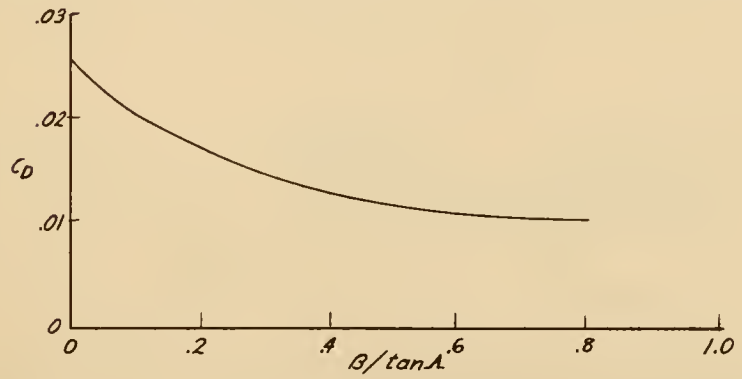

(c) Configuration drag.

Figure 10.- An example of the calculation of the configuration drag from the drag of the area distributions at various values of $\beta \cos \theta/\tan \Lambda$. 60° delta wing; NACA 65A006 airfoil section.

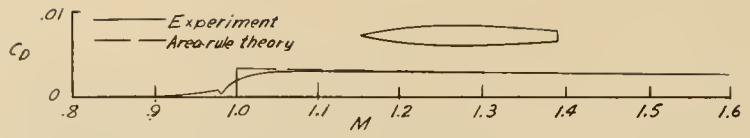

(a) Basic body; model 1 (ref. 16); $\frac{Sb}{Sw} = 0.0305$.

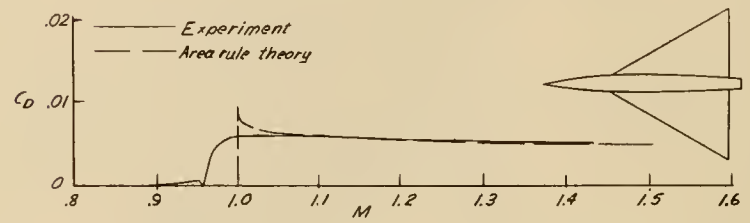

(b) Model 4 (ref. 16); 60° delta wing; NACA 65A003 airfoil section; $\frac{Sb}{Sw} = 0.0305$.

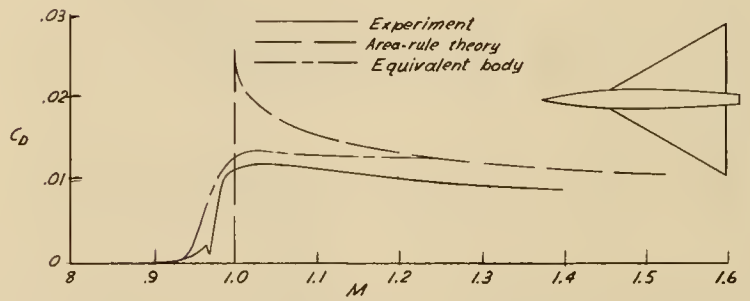

(c) Model 5 (ref. 16); 60° delta wing; NACA 65A006 airfoil section; $\frac{Sb}{Sw} = 0.0305$.

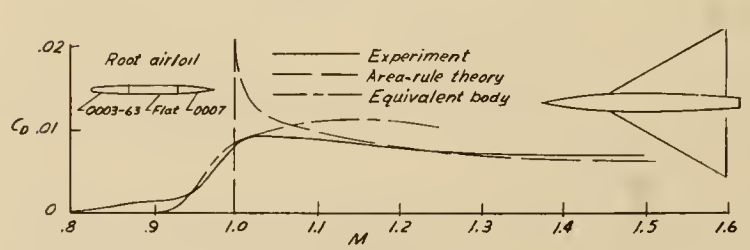

(d) Model 6 (ref. 19); 60° delta wing. Thickness ratio varies from 0.03 at root to 0.06 at 0.9 semispan. $\frac{Sb}{Sw} = 0.0305$.

Figure 11.- Comparison of the calculated drag with experiment and equivalent-body test results for wing-body combinations.

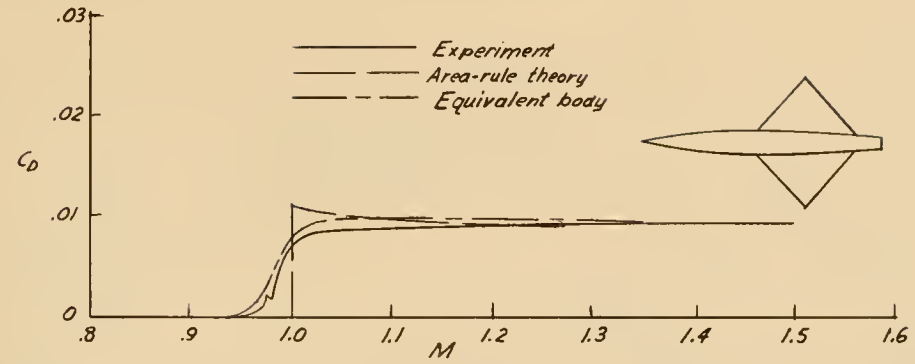

(e) Model of reference 17; A = 2.31; $\Lambda_c/2 = 0$; NACA 65A003 airfoil section; $\frac{Sb}{Sw} = 0.0606$.

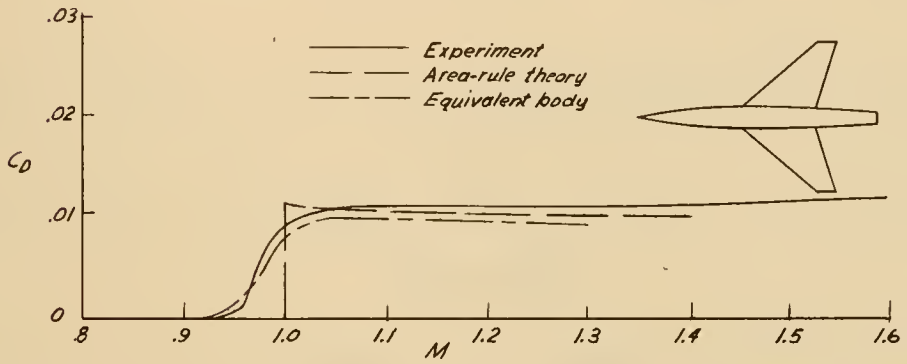

(f) Model C-3 (ref. 18); A = 3; $\lambda = 0.2$; $\Lambda_c/4 = 45°$; NACA 65A003 airfoil section; $\frac{Sb}{Sw} = 0.0606$.

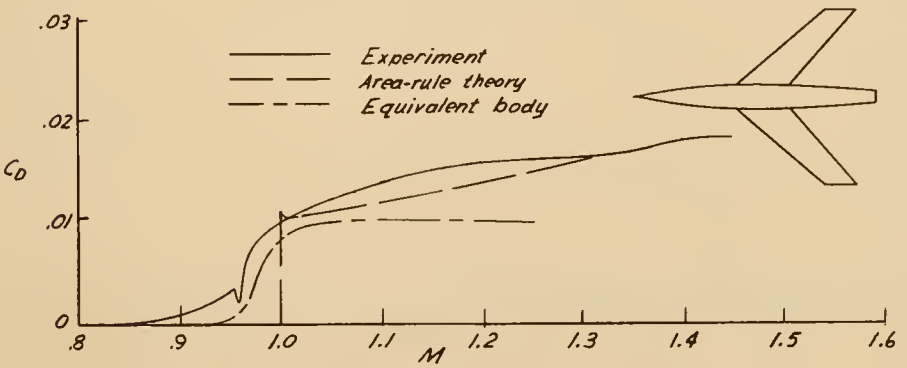

(g) Model 6 (ref. 16); A = 4; $\lambda = 0.6$; $\Lambda_c/4 = 45°$; NACA 65A006 airfoil section; $\frac{Sb}{Sw} = 0.0606$.

Figure 11.- Continued.

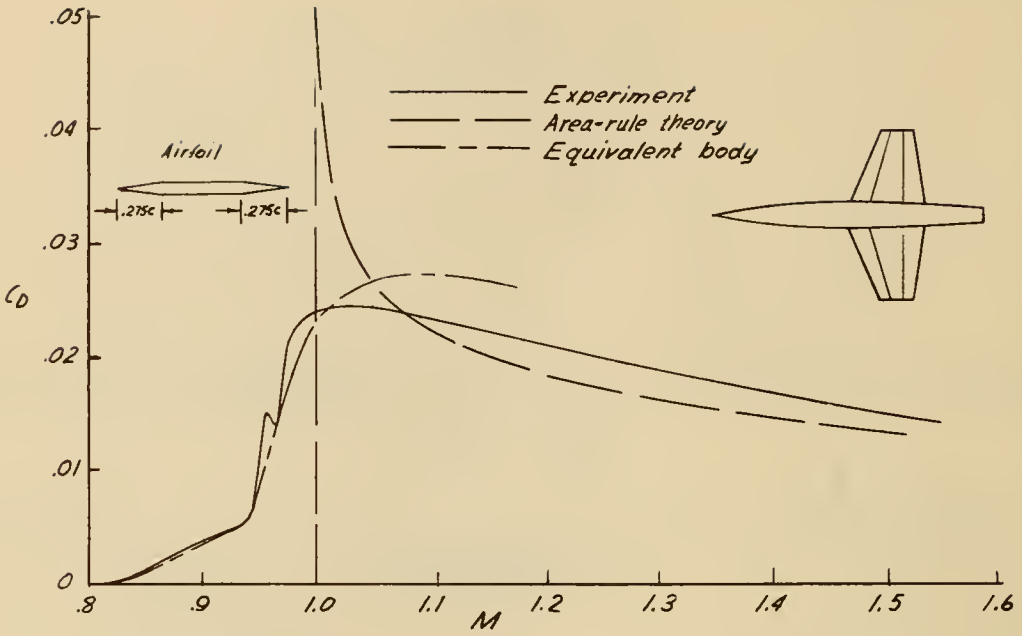

(h) Model 2 (ref. 16); A = 3.04; λ = 0.394; $\Lambda_{3c/4}$ = 0°; $\frac{t}{c}$ = 0.045;

$\frac{Sb}{Sw}$ = 0.0606.

Figure 11.- Concluded.

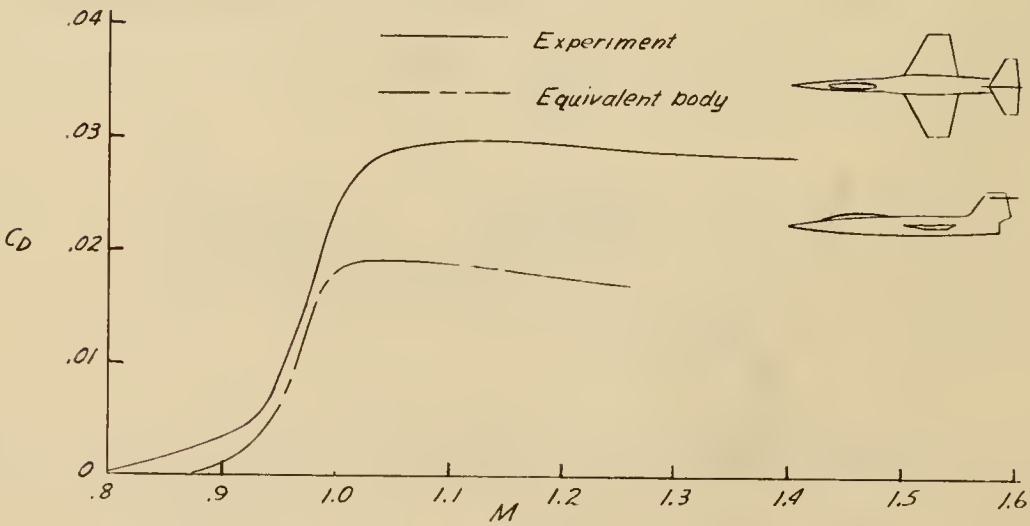

Figure 12.- Comparison of equivalent-body drag and configuration drag for an airplane configuration.

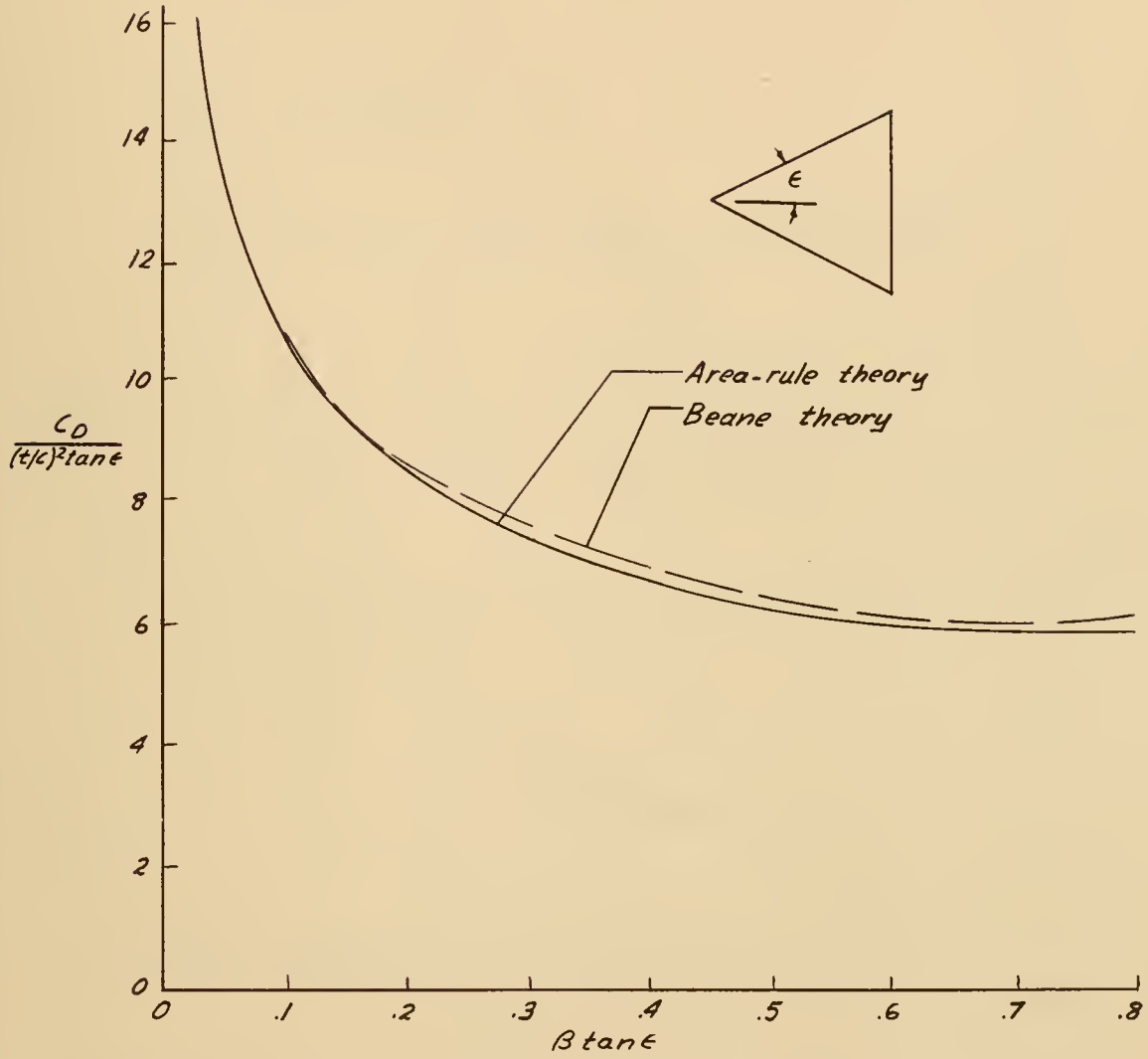

Figure 13.- Comparison of the drag of delta wings calculated with two versions of the linearized theory.

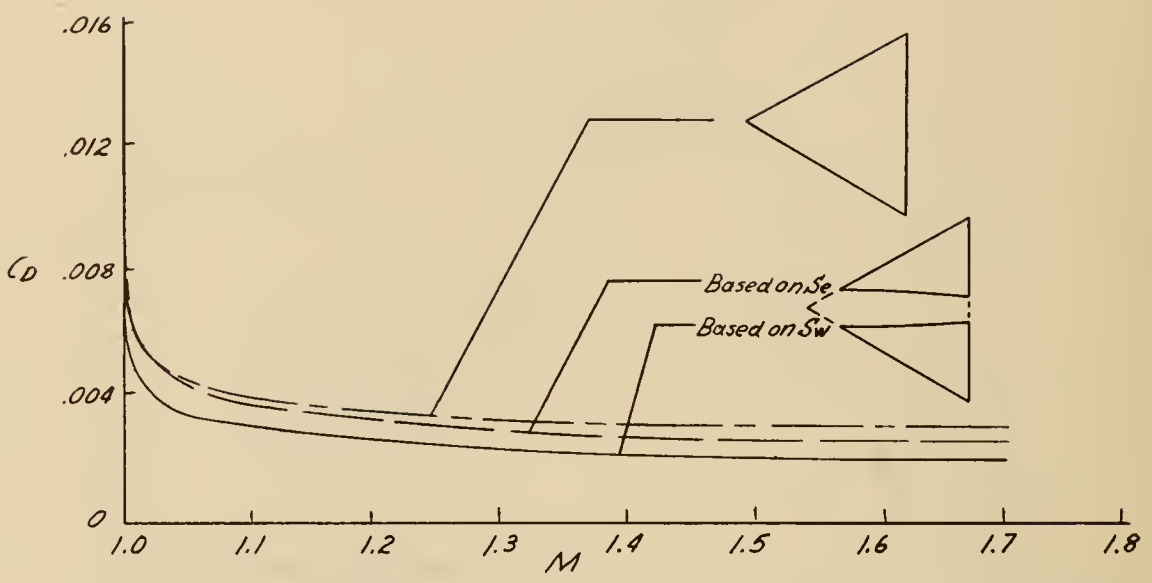

Figure 14.- Effect of wing-panel separation on wing drag. 60° delta wing; NACA 65A003 airfoil section.

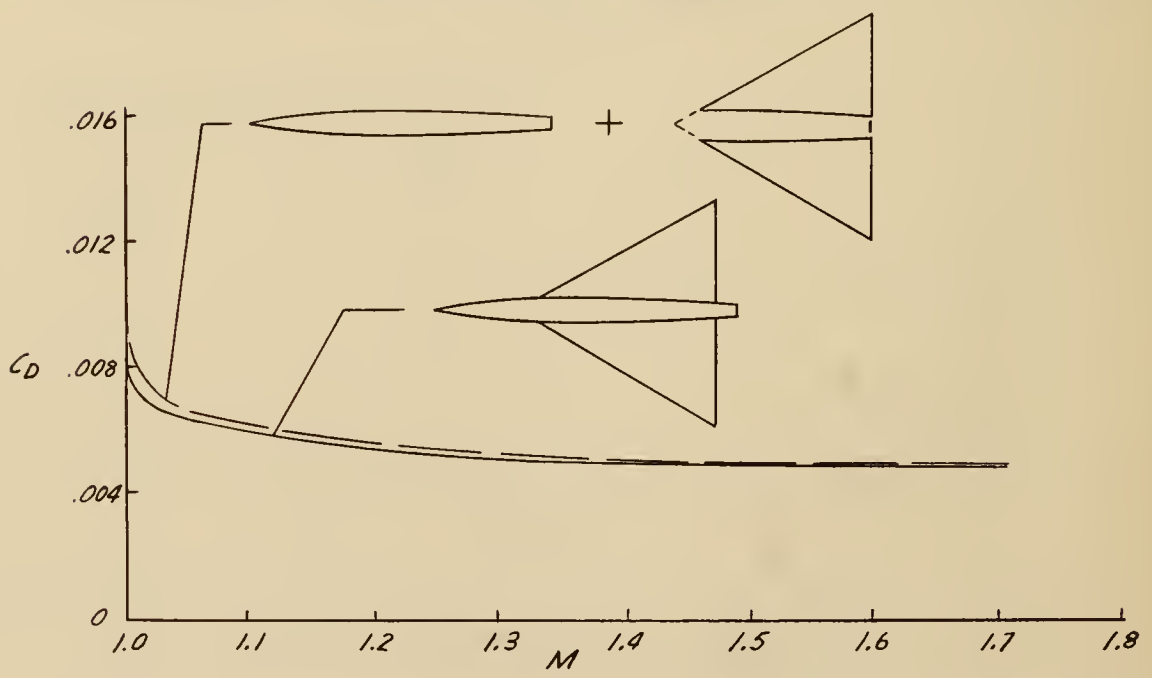

Figure 15.- Comparison of the sum of component drags with the configuration drag. 60° delta wing; NACA 65A003 airfoil section.

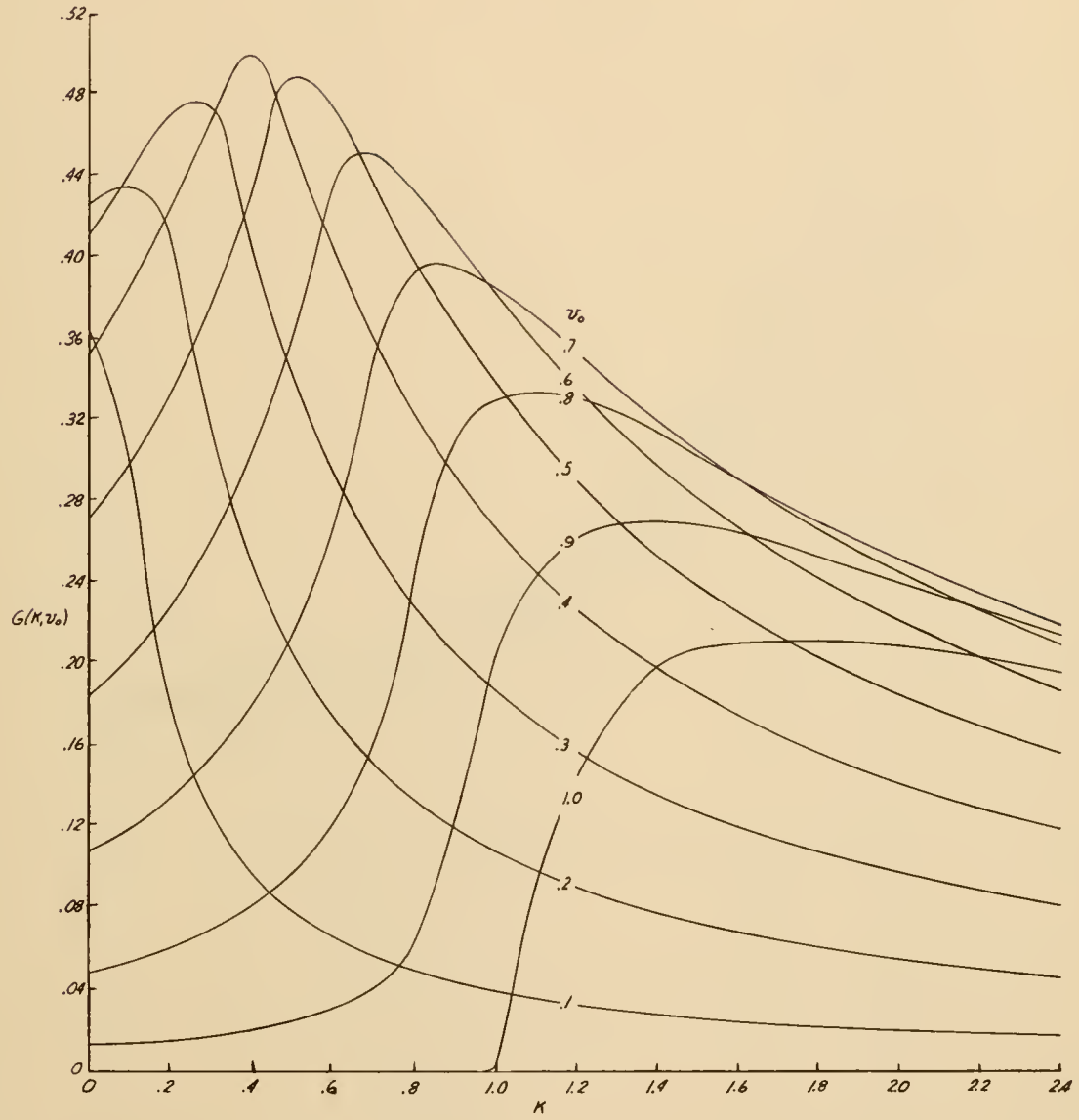

Figure 16.- Area distribution parameter $G(K, v_0)$ for 65A series airfoil.

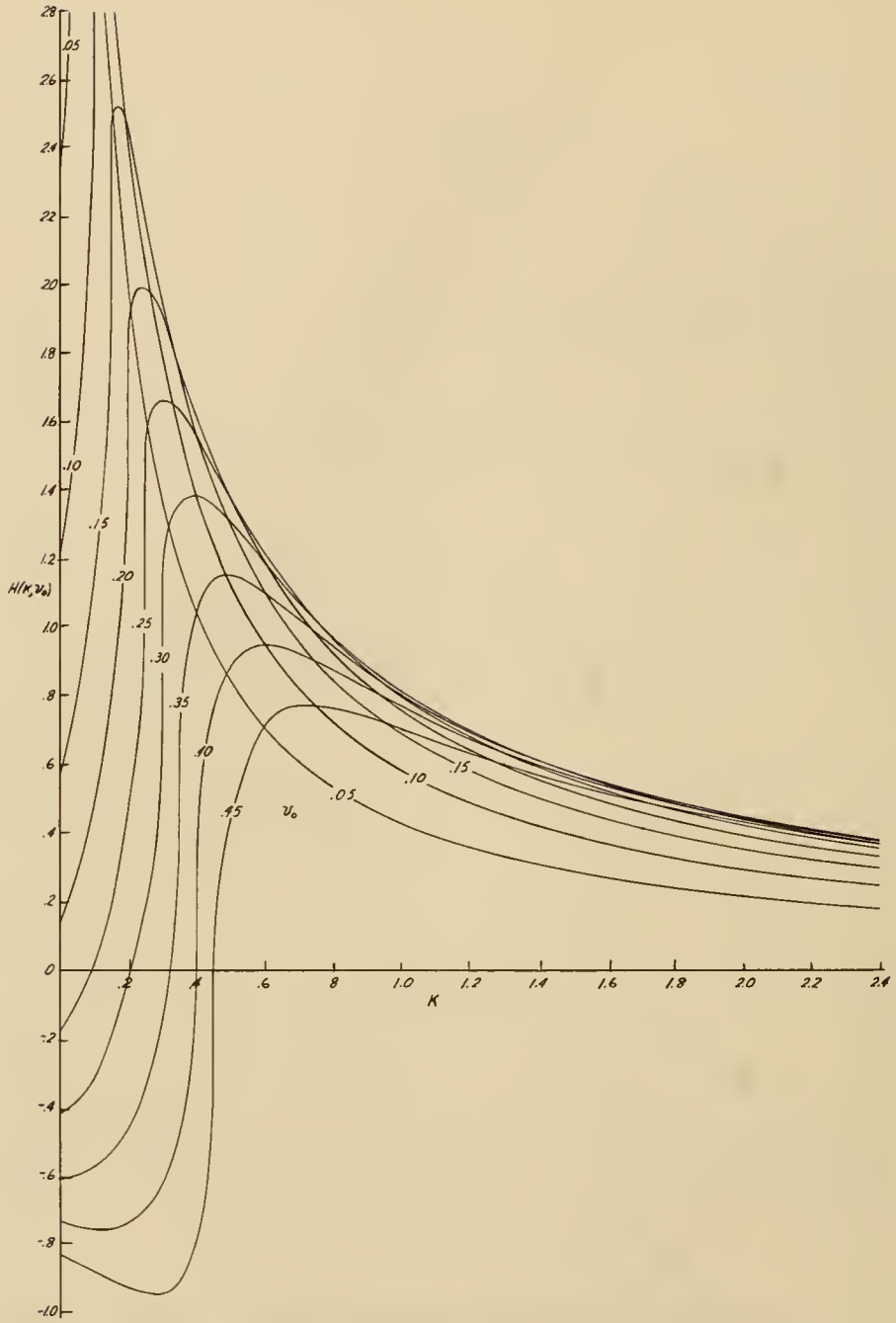

(a) ν_0 from 0 to 0.45.

Figure 17.- Area-distribution-slope parameter $H(K, \nu_0)$ for 65A series airfoil.

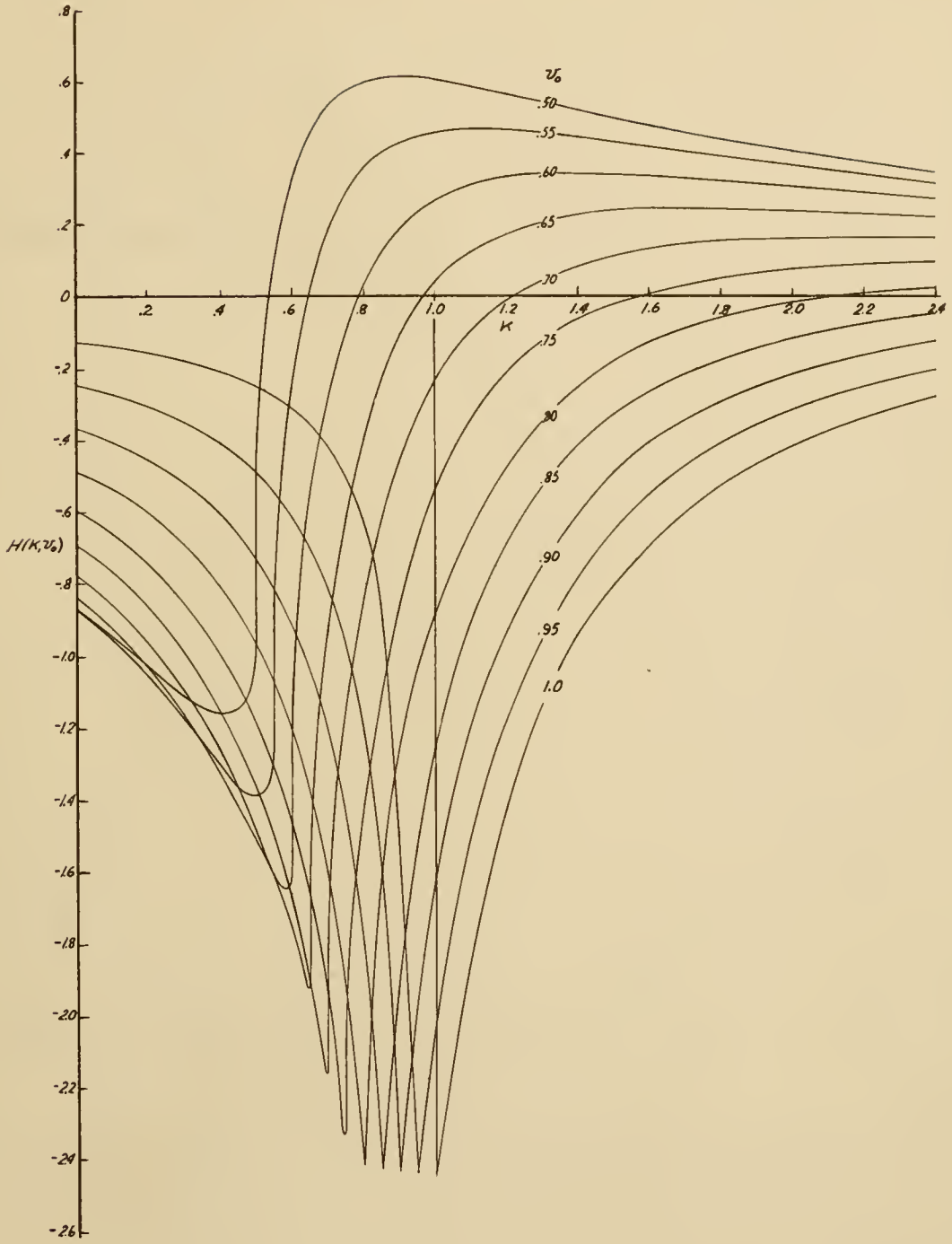

(b) v_0 from 0.5 to 1.0.

Figure 17.- Concluded.

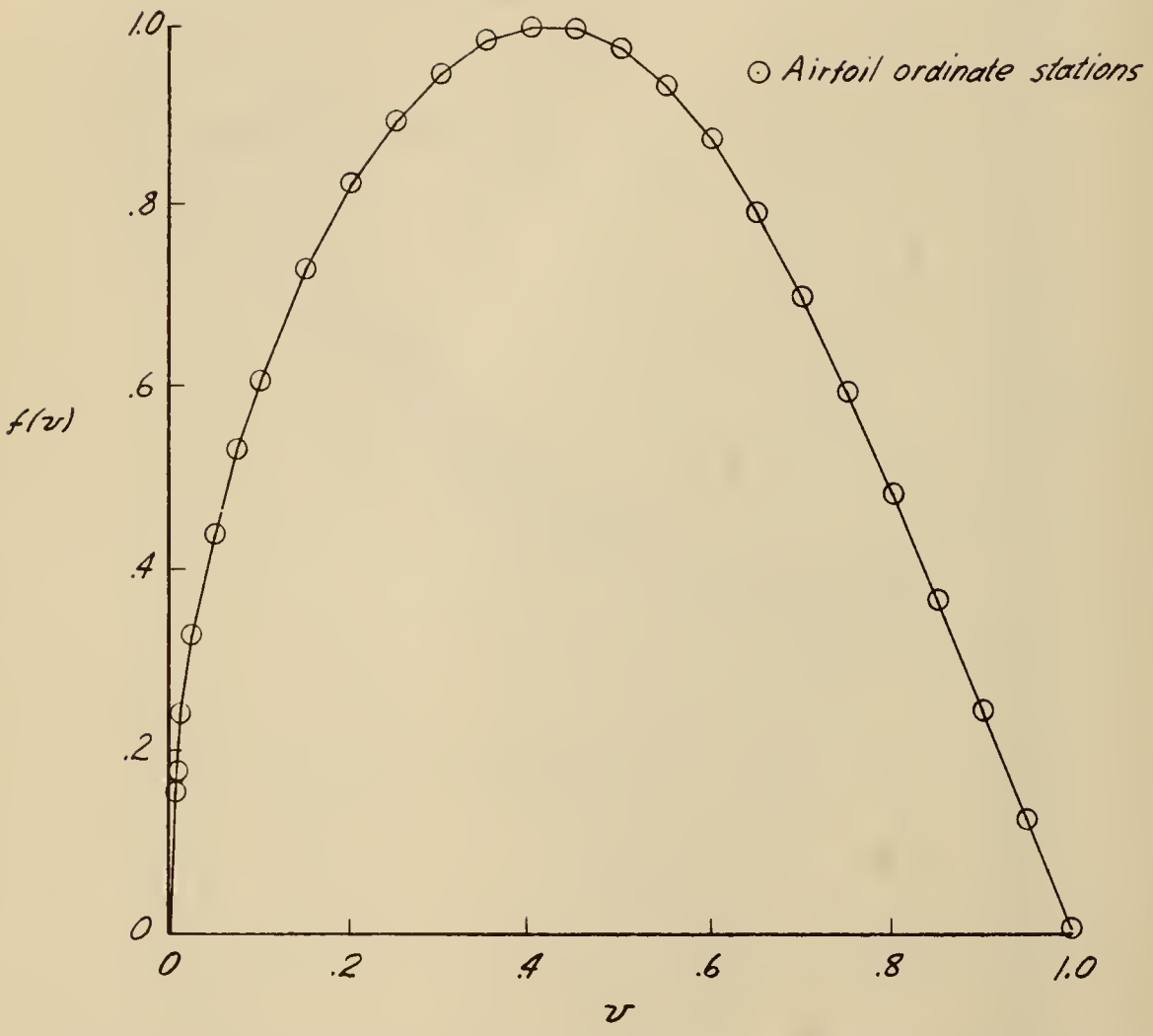

Figure 18.- Approximation of 65A series airfoil for the calculation of $G(K, \nu_0)$ and $H(K, \nu_0)$.

NACA - Langley Field, Va.

CONFIDENTIAL

CONFIDENTIAL